Energy and exergy analysis of microchannel central solar receivers for pressurised fluids

D. D'Souza[a,b], M.J. Montes[a,b], M. Romero[a] and J. González-Aguilar[a,&]

[a] High Temperature Processes Unit, IMDEA Energy, Avda. Ramón de la Sagra 3, 28935, Móstoles, Spain

[b] E.T.S. Ingenieros Industriales - UNED, C/Juan del Rosal 12, 28040 Madrid, Spain

[&]Corresponding author: J. Gonzalez-Aguilar, jose.gonzalez@imdea.org

Abstract

Within the new generation of advanced central solar receivers, microchannel pressurised gas receivers are emerging as reliable and efficient alternatives to operate at high temperatures and pressures. This paper presents an optimisation and comparative analysis of different compact plate-fin type structures, constituting the receiver's absorber panels, classified according to the type of fin arrangement inside: plain rectangular, plain triangular, wavy, offset strip, perforated, and louvred fin. A versatile thermo-fluid receiver model is implemented, allowing simple variation of characteristic geometric parameters of each structure. Exergy efficiency is chosen as the optimisation function, as it considers both heat and pressure losses.

The framework of the analysis is set by the receiver's boundary conditions, operating at the design point conditions of a solar thermal power plant. For each compact structure, the optimal configuration is determined, providing interesting findings that have not been reported in the state-of-the-art to date. Although all geometries show good thermal performance, the perforated and plain rectangular configurations demonstrate the best exergy efficiencies of 59.21% and 58.80%, respectively, favouring taller and narrower channels. This analysis methodology could be seamlessly extrapolated to other gases and working conditions, owing to the thermo-fluid model's versatility, to reveal the optimal configuration for each case.

Keywords

Microchannel; pressurised fluids; solar receiver; solar thermal power; energy efficiency; exergy efficiency.

Acronyms

CHE	Compact Heat Exchanger
CST	Concentrated Solar Thermal
CSP	Concentrated Solar Power
CFD	Computational Fluid Dynamics
EA	Electrically Assisted
EDM	Electrical Discharge Machining
HCE	Heat Collector Element
HTF	Heat Transfer Fluid
HX	Heat Exchanger
IRENA	International Renewable Energy Agency
LCOE	Levelized Cost of Electricity
LF	Louvred Fin
LMTD	Log Mean Temperature Difference
NIST	National Institute of Standards and Technology
NREL	National Renewable Energy Laboratory
OSF	Offset Strip Fin
PCHE	Printed Circuit Heat Exchanger
PF	Perforated Fin
PGR	Pressurised Gas Receiver
PFHE	Plate Fin Heat Exchanger
PHE	Plate Heat Exchanger
PRF	Plain Rectangular Fin
PTF	Plain Triangular Fin
RNM	Resistance Network Model
RPC	Reticulated Porous Ceramic
sCO_2	Supercritical Carbon Dioxide
SCR	Solar Central Receiver
SHE	Spiral Heat Exchanger
SLM	Selective Laser Melting
STPP	Solar Thermal Power Plant
TRM	Thermal Resistance Model
WF	Wavy Fin

NOTATION

Latin letters

A	Area (m^2)
B	Breadth (m)
c_p	Specific heat at constant pressure (J kg^{-1} K^{-1})
D	Diameter (m)
F	View factor
f_D	Darcy pressure friction loss factor
f_F	Fanning pressure friction loss factor
h	Specific enthalpy (J kg^{-1})
H	Height (m)
h_{conv}	Convection heat transfer coefficient (W m^{-2} K^{-1})
j	Colburn factor
k	Thermal conductivity (W m^{-1} K^{-1})
L	Length (m)
M	Mass (kg)
$\dot{m}$	Mass flow rate (kg s^{-1})
N	Number of channels/elements
Nu	Nusselt number
ΔP	Pressure Drop (Pa)
p	Pitch (m)
P	Pressure (Pa)
Pr	Prandtl number
$\dot{Q}$	Thermal power (W)
r	Radius (m)
R	Thermal Resistance (K W^{-1}), Ideal gas constant (J kg^{-1} K^{-1})
Re	Reynolds number
t	Channel wall thickness (m)
T	Temperature (K)
U	Overall heat transfer coefficient (W m^{-2} K^{-1})
v	Velocity (m s^{-1})
V	Volume (m^3)

Greek Letters

η	Efficiency
ρ	Density (kg m^{-3})
μ	Dynamic viscosity (Pa s)

Δ	Differential
δ	half angle of the cone subtended by the sun's disc (rad)

Subscripts

0	Base case
abs	Absorbed
amb	Ambient
ap	Aperture
avg	Average
b	Base wall
c	Channel
cond	Conduction
conv	Convection
e	Element, electrical
h	Hydraulic, horizontal
in	Inlet
loss	Loss
net	Net
opt	Optical
out	Outlet
p	Pressure, plate
rad	Radiation
rec	Receiver
ref	Reflection
th	Thermal
v	Vertical
w	Wall

1. Introduction

According to IRENA, the weighted average Levelized Cost Of Electricity (LCOE) of Concentrating Solar Power (CSP) has decreased between 2010 and 2020 from USD 0.34/kWh$_e$ to USD 0.108/kWh$_e$ [1]. This LCOE reduction over the last decade has been mainly due to the lowering of CSP installation costs, which in 2020 became 50% cheaper than in 2010, owing to greater economies of scale. Nevertheless, if the target of USD 0.06/kWh$_e$ is to be achieved [2], it is essential to increase the global thermal performance of Solar Thermal Power Plants (STPPs). To this end, the Gen3 CSP Roadmap established three development pathways for central receiver technology on the basis of the Heat Transfer Fluid (HTF) employed: molten salts, particles, and gas-phase fluids [3].

Within these three pathways, the technology most developed and commercialised is based on molten salts. An overarching objective for the next generation of CSP plants, across all receiver development pathways, is an increase in the receiver outlet temperature, from the conventional 565 °C to 700 °C, to increase power cycle efficiency [4],[5],[6]. This, however, brings significant technical challenges in molten salts, mainly related to chemical instability and material corrosion [7]. Regarding particle receivers, they can stably operate at high temperatures, up to 1,000 ºC, and inherently permit direct storage, but their main drawback lies in the downstream primary heat exchanger between the particles and the working fluid in the power cycle. Particle conveyance, attrition and transport also remain a challenge for these receivers [8],[9]. At last, gas-phase receivers can operate at high temperatures (>1,000 °C) in general, and they are stable across a wide temperature range besides being cheaper, less corrosive than commercial molten salts and non-environmentally hazardous [10]. However, there are several challenges to its widespread adoption including difficulties in thermal storage, higher pressure drops (leading to larger fluid circulation power demands) and poor performance when a gas is used as HTF due to its unfavourable thermo-physical properties. The poor heat evacuation also limits the operation temperature of solar receivers since their solid surfaces may not be cooled sufficiently [11]. Within gaseous fluid receivers, Pressurised Gas Receivers (PGRs) offset some of the inherent disadvantages of gas phase receivers by ensuring that there is adequate mass flow in all channels and avoiding flow instabilities characteristic of volumetric receivers [12],[13],[14]. Besides, if the gas is pressurised, the pressure drop is reduced for the same mass flow and cross section as density is approximately proportional to pressure, thus the velocity is much lower at high pressure. Additionally, HTF is not limited to air, which is the case with atmospheric gas receivers and other gases with more favourable heat transfer characteristics may be used [15]. Pressurised gas receivers may be further classified on the basis of the gas employed (air, helium, nitrogen, etc.), the irradiation conditions (directly, indirectly or hybrid) and the flow path geometry [16]. With respect to their internal geometry, tubular receivers are by far the most studied and developed [17],[18],[19], though alternative concepts exist such as the embedded channel receiver [20], impinging jet receiver [21],[22],[23], Reticulated Porous Ceramic (RPC) lined cavity receivers [24],[25],[26] and microchannel receiver [27],[28].

Microchannel pressurised gas receivers, which are the focus of this study, seek to achieve the objective of improving the heat transfer to the gaseous fluid by increasing the heat transfer area for the same receiver volume, and improving the convection heat transfer coefficient due to decreased diffusion length compared to conventional channels or tubes [29]. Within the microchannel receiver concept, the use of a pressurised gas is advisable to reduce the pressure drop and flow instabilities, as explained previously. Microchannel receivers, as the name suggests, consist of miniature channels. The inspiration for such receivers comes on the back of growth in Compact Heat Exchanger (CHE) technologies (cf. Annex A.1) and their increased real-world application [30],[31]. The reduction in channel size, i.e. compactness of CHEs, results in a volume reduction for the same effective heat transfer area; higher heat transfer coefficients; and higher pressure drop, although this effect could be offset by using pressurised fluids.

A review into the suitability of different CHE geometries for solar receivers led to the development of a microchannel receiver prototype [27],[28], which was divided into 12 parallel channels with each channel being 1 mm wide and 3 mm high. Rectangular ribs were attached on top of each channel. These ribs had the same width as the channel and a height and pitch of 2 mm and 1 mm, respectively. The first rib was placed just at the entrance of the air passage. The receiver was manufactured of Inconel 625 using Selective Laser Melting (SLM). The outer (or top) surface of 30 mm × 30 mm was the irradiated plane. Experiments were carried out using pressurised air (2-6 bar) and resulted in a thermal efficiency of around 64% with a pressure drop of around 750 mbar. Another interesting microchannel prototype based on structures commonly used in a Plate Fin Heat Exchanger (PFHE) was developed and numerically analysed in [32–34]. This 3 MW_{th} receiver, made of Inconel 625, consists of several plates joined by diffusion with rectangular fins and square-shape channels. It was designed to heat supercritical CO_2 (sCO_2) from 530 ºC to 700 ºC at 20 MPa. In the same work, a parametric analysis was also carried out to study the effect of the hydraulic diameter, number of vertical rows, and channel thickness on the thermal resistance and pressure drop. It was observed that the thermal resistance was directly related to the hydraulic diameter and number of vertical rows, whereas the pressure drop indirectly so. Increasing the channel thickness slightly reduced the thermal resistance, but it leads to a more substantial increase in the pressure drop as the receiver breadth was fixed. On a much smaller scale, absorber panels with a PFHE structure and channel sizes in the order of hundreds of micrometres were manufactured using Electrical Discharge Machining (EDM) [35],[36]. Haynes 230 was chosen as the receiver material. Lab-scale absorber panels of 2 cm × 2 cm were made and proven to absorb 100 W cm^{-2} of incident flux using sCO_2 at 650 ºC and 80-200 bar as working fluid, reporting thermal efficiencies around 90%. Finally, a recent sCO_2 receiver prototype using the PFHE concept has been developed in the National Renewable Energy Laboratory (NREL). In this 2 MW_e design, the compact structure consists of two attached plates with a wavy fin arrangement between them; these plates act as the absorber surfaces of the concentrated solar radiation and they are arranging forming a cavity [37]. Several studies have investigated the shape of similar cavity receivers, optimising the geometries and configurations, with the aim of improving the performance of the receiver by reducing the radiation and convection losses from its surface [38],[39],[40],[41]. High fin density (up to 32 fins/cm) and thin walls were expected to improve the heat transfer besides providing crucial mechanical support against high internal pressures (25 MPa). The receiver, and its individual panels, were constructed of Inconel 625 and was predicted to have an efficiency of around 90%. A 10 MW_e receiver based on this concept has been designed and simulated. In this last case, the absorber plates were arranged to form an external cylindrical receiver.

The state of the art shows that, to date, very few varieties of CHE sub-structures or internal flow geometries have been investigated, namely the plain square/rectangular fin type structure [32], the pin fin structure [35] and the wavy fin type structure [37]. However, there are several other potential CHE internal flow structures that have neither been individually analysed nor collectively compared in the context of their application to solar receivers. In this regard, this paper aims at conducting an in-depth study of those potential geometries for microchannel receivers using pressurised gas. The manuscript is organised as follows. The overall framework within which the analysis is performed is laid out in section 2. For a proper comparative analysis, it is imperative to set a suitable operational framework and boundary conditions for the receiver. These operating conditions are detailed in section 2.1, when describing the global STPP based on the microchannel pressurised gas receiver. After establishing these boundary conditions, the sizing and operating conditions of the receiver subsystem are set out in section 2.2. The geometrical characterisation of the different compact structures, as well as the scope of the parametric study, are presented in section 2.3. Having defined the global operational structure, section 3 presents the thermo-fluid dynamic model developed and aspects pertaining to its application in this analytical work. The numerical model used to analyse and compare the various CHE geometric structures is detailed in section 3.1 followed by its validation in section 3.2. The selection of appropriate performance indicators is important to any comparative and optimisation analysis and this is dealt with in section 3.3. Section 4 is devoted to the results including an analysis of the performance and behaviour of the different receiver types in section 4.1, and finally a comparative analysis is elucidated in section 4.2. Exergy efficiency is identified as a suitable figure of merit as it considers the exergy increase associated to the fluid heat gain, and the exergy decrease caused by the pressure drop and the heat loss. The results present the optimal geometric parameters for each compact structure and the comparison between optima. At last, section 5 summarises the main conclusions, as well as future research lines.

2. Framework for microchannel receiver analysis

2.1. Layout and nominal conditions of solar thermal power plant

The performance analysis of a solar receiver primarily requires an adequate framework, which is fixed by the overall STPP performance at design point. The operating conditions of the receiver are firstly imposed by the useful thermal power required by the thermal cycle. Although this pressurised receiver can be coupled to several power cycles, a sCO_2 power cycle has been considered following a layout similar to that depicted in Figure 1.

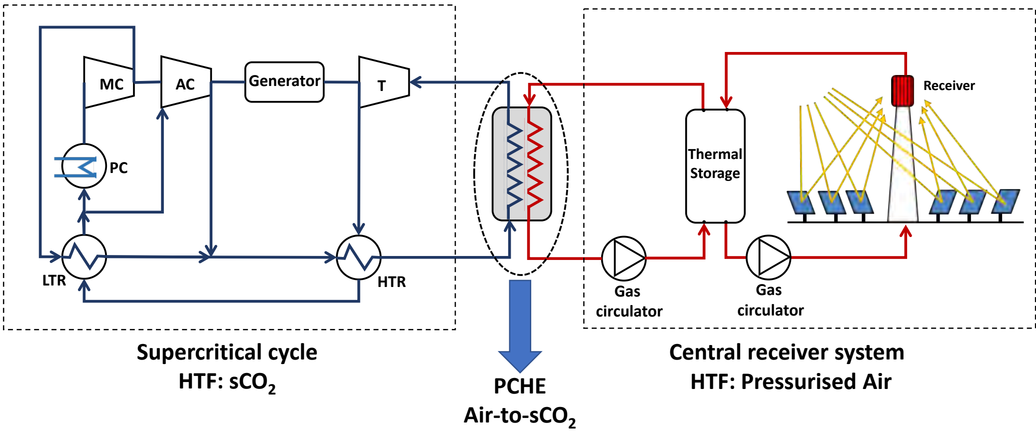

Figure 1. Scheme of a STPP based on a pressurised air central receiver coupled to a supercritical CO_2 power cycle

As shown in Figure 1, the supercritical layout selected is the conventional recompression thermodynamic cycle. The cycle power output has been set at 10 MW_e with a solar multiple of 1.5. An electrical power of 10 MW_e is considered representative for an initial prototype that will later be scaled to a commercial level. The isentropic efficiencies of both the turbine and the compressors have been set at 92% and 88%, respectively; a dry cooling by means of a precooler is assumed; and the sCO_2 pressure and temperature at the turbine inlet are 200 bar and 688 ºC, respectively. At these conditions, the nominal thermal efficiency is 49.57%, thus the thermal power required in the primary heat exchanger is 20.17 MW_{th} [42]. Assuming a thermal efficiency in the source heat exchanger equal to 98%, and considering the solar multiple previously mentioned, the total thermal power in the central solar receiver is 30.26 MW_{th}. The heat transfer fluid in the proposed receiver is pressurised air. The air temperatures at the inlet and outlet of the solar receiver are also determined by the power cycle conditions. Specifically, if the source heat exchanger is assumed to be balanced and the temperature difference between the two fluid streams is constant and fixed at 12 ºC, then the inlet and outlet air temperatures are 557.6 ºC and 700 ºC, respectively. The air pressure at the receiver inlet is taken as 25 bar. Since the pressure difference between sCO_2 and pressurised air streams is high, a PCHE, which is capable of operating under such conditions, is recommended for use as the HX, coupling the solar field to the power cycle with previous studies having undertaken such design studies [42].

For the receiver simulation model, the thermodynamic properties of the pressurised air have been sourced from the NIST database [43], for temperature steps below 1.5 ºC and pressure steps of roughly 1 mbar. Furthermore, assumed environmental conditions are the ambient temperature at 25 ºC, the sky temperature at 15 ºC and the wind speed equal to 1 m/s.

2.2. Configuration and characteristics of microchannel solar receiver

Before making a performance analysis of the various compact structures, it is first necessary to define an overall receiver structure. As shown in Figure 2, an external cylindrical receiver configuration has been defined having 20 rectangular panels in a parallel configuration, uniformly irradiated, through which pressurised air flows in a single pass. These absorber panels (henceforth referred to as absorbers) are assembled so as to form 2 vertical rows of 10 cylindrically arranged absorbers. CHE structures are implemented in each absorber. Cold air enters from a common inlet manifold, located between the two rows, before splitting into the individual absorbers. This configuration is similar to the one adopted for the sCO_2 receiver proposed by NREL [37].

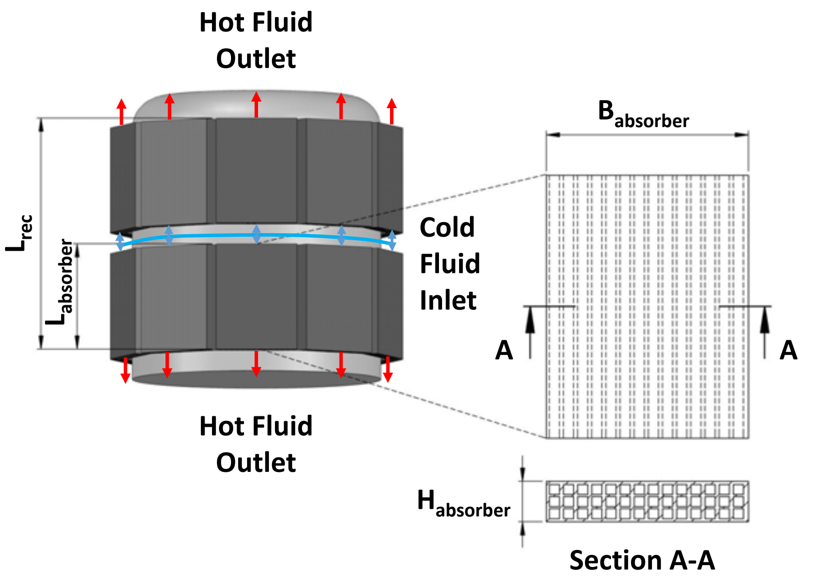

Figure 2. Receiver configuration, i.e. external cylindrical like receiver comprised of 20 parallel rectangular absorber panels arranged cylindrically in 2 vertical rows.

Inconel 617 has been selected as the receiver material because of its machinability and high temperature corrosion resistance [44],[45]. Deferring to the state of the art [46],[47], the receiver aspect ratio (receiver length to diameter ratio) is fixed at 0.7 with the maximum and minimum mean incident fluxes set at 800 kW m^{-2} and 400 kW m^{-2}. These along with additional operation boundary conditions, summarised in Table 1, are used to size the absorbers and, in turn, the overall receiver in an iterative process which is detailed in Section 2.4.

Table 1. Operational boundaries conditions of pressurised air receiver.

Parameter	**Unit**	**Operating Limits**	
		Minimum	**Maximum**
Mean incident flux	kW m^{-2}	400	800
Channel velocity	m s^{-1}	-	50
Outer surface temperature	ºC	-	800
Absorber temperature gradient (outer to back surfaces)	ºC	-	200
Reynolds number	-	10^4	-

The temperature gradient from the absorber's external irradiated surface to the back is expected to be high given the low thermal conductivity of Inconel 617 [44] and the generally poor heat transfer characteristics of air; hence the addition of an upper limit to this temperature gradient as well as mean incident flux which are both presented in Table 1. As a consequence of air's low density, the absorber cross section area, directly related to the absorber breadth and hence receiver diameter, required for a given absorber mass flow rate and channel velocity is relatively high. Keeping this in mind, the number of absorbers in parallel (which determines the mass flow rate in each absorber) and the bounds of mean incident flux have been set to maintain a reasonable receiver aspect ratio. Given that the absorbers tend to broader and shorter dimensions, stacking the absorbers one above the other mitigates, to an extent, the low receiver aspect ratio issue by effectively doubling the receiver length.

For the working temperatures considered in this study (above 700 ºC), a cavity type receiver is most recommended to reduce radiation heat losses [46]. Nevertheless, there is a recent research line that seeks to decrease the radiation losses by the reduction of the view factors, using microscopic or macroscopic geometries that would act as solar traps [8],[48]. At the microscopic scale, the external receiver proposed in this paper has adopted the configuration developed by NREL for their pressurised microchannel receiver [37], as mentioned in the state of the art review. This design employs cylindrical quartz tubes attached perpendicularly to its external surface, in such a way as to reduce the view factor and the convective losses.

For the external receiver proposed in this work, cylindrical quartz tubes with an aspect ratio (height-to-diameter ratio) of 0.5 are considered. The view factor of this cavity is calculated using a conventional formula for parallel circular disks with centres along the same normal [49],

$$F_{rec-ap} = \frac{1}{2}\left[X - \sqrt{X^2 - 4\left(\frac{R_2}{R_1}\right)^2}\right],\qquad (1)$$

where $X = 1 + \frac{1+R_2{}^2}{R_1{}^2}$, $R_1 = \frac{r_1}{L}$, $R_2 = \frac{r_2}{L}$; r_1/r_2 and L are the quartz cylinder radius and length, respectively. Assuming $R_1 = R_2 = 1$, $X = 3$ and the view factor is $F_{rec-ap} = 0.382$, which is the value introduced in the program.

It is important to point out that this estimation of the view factor can be varied if different configurations are adopted as solar traps, the emissivity value may also be changed if different materials are considered. One of the advantages of the simulation model developed is its versatility to adapt to many designs. A summary of the proposed receiver model and its working conditions are presented in Table 2.

Table 2. Summary of the main thermal and geometric parameters of the pressurised air receiver.

Parameter	**Unit**	**Value**
Material	-	Inconel 617
Inlet temperature	°C	557.6
Outlet temperature	°C	700
Inlet pressure	bar	25
Mass flow rate	kg s^{-1}	191.49
Receiver area	m^2	63.44
Receiver length	m	3.79
Receiver diameter	m	5.41

2.3. Characterisation of compact structures forming flow channels of absorber panels

The selected CHE channel geometries, for the internal flow paths of each absorber, analysed and compared in this work are the following [50]: Plain Rectangular Fin (PRF), Plain Triangular Fin (PTF), Wavy Fin (WF), Offset Strip Fin (OSF), Perforated Fin (PF) with rectangular cross-section, and triangular shaped Louvred Fin (LF). These geometries are presented in Figure 3.

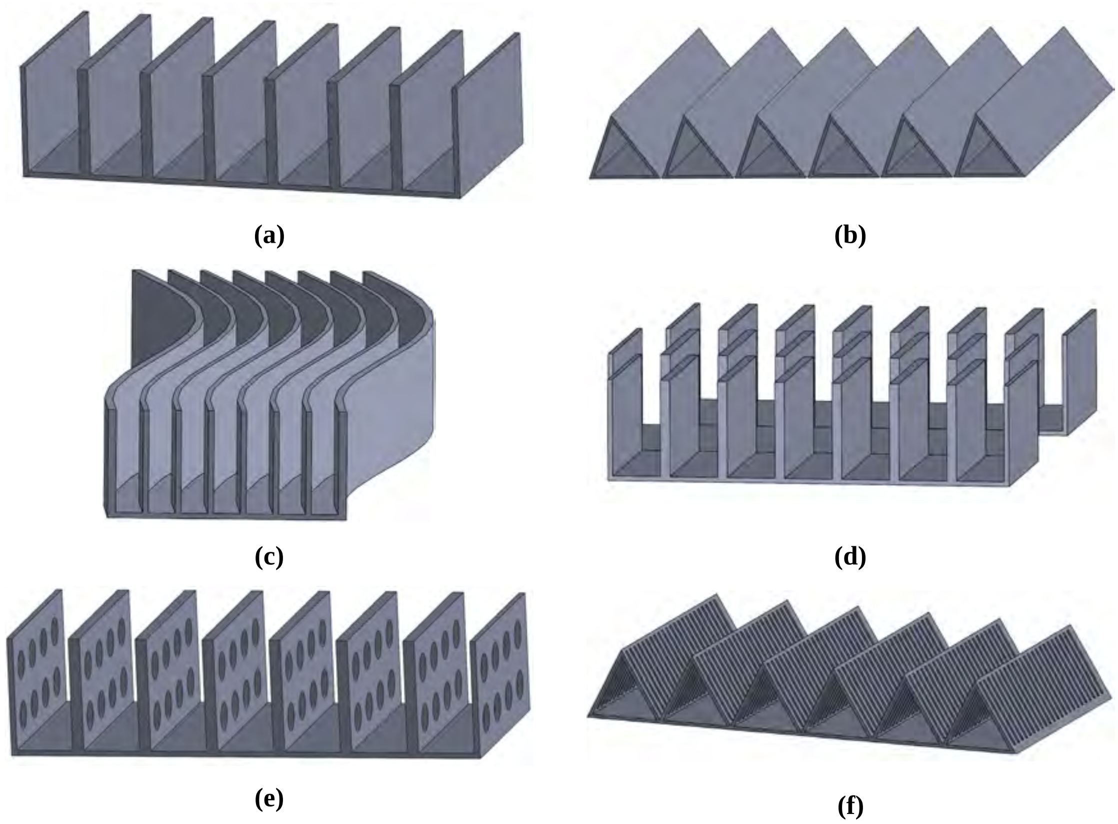

Figure 3. CHE channel geometries analysed in the pressurised air receiver model. (a) Plain Rectangular Fin (PRF); (b) Plain Triangular Fin (PTF); (c) Wavy Fin (WF); (d) Offset strip Fin (OSF); (e) Perforated (Rectangular) Fin (PF); and (f) Louvred (Triangular) Fin (LF).

The channel geometries presented in Figure 3 can be characterised by common parameters. Identifying these parameters and studying the effects of their variations will allow for an optimisation analysis that reveals the best parameter set for each channel geometry type. Besides, the analysis also facilitates a comparison among the different receivers, each with different channel geometries. Four parameters, common to all channel geometries, have been identified as the most crucial and these are the channel height (H_c), channel breadth (B_c), channel wall thickness (t) and the number of vertical channels or rows (N_{cv}). Note that the thicknesses of the walls separating horizontally and vertically adjacent channels are taken as identical (t).

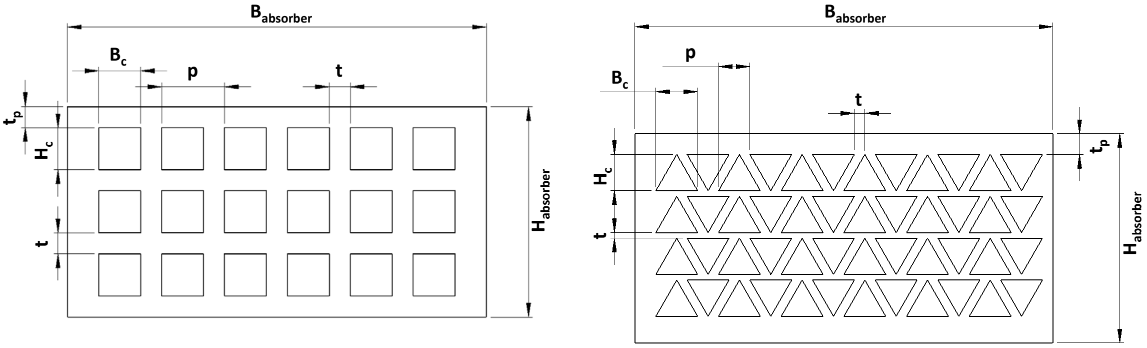

Figure 4. Channel geometrical parameters for rectangular fin (left) and triangular fin (right) receivers.

All the channel geometries are either rectangular or triangular shaped channels when viewed from the flow inlet/outlet. Figure 4 depicts the geometric parameters defining these structures including the previously defined constant absorber breadth ($B_{absorber}$) besides derived parameters such as the channel pitch (p) and absorber height ($H_{absorber}$), both of which are calculated after defining the four variable parameters.

The parametric study varying the four parameters uses the datapoints presented in Table 3 and all combinations of the variables are fed into the simulation model. It should be noted that for the LF geometry, H_c and B_c were initiated at 7 mm as excessive pressure drops were observed at lower values.

Table 3. Parametric study performed for optimisation analysis.

Parameter	Unit	Studied Parameter Values				
H_c	mm	$6.00^{\&}$	8.25	10.50	12.75	15.00
N_{cv}	-	3	5	7	8	10
B_c	mm	$6.00^{\&}$	8.25	10.50	12.75	15.00
t	mm	1.00	1.50	2.00	2.50	3.00

[&]For the LF geometry, H_c and B_c are initiated at 7 mm to avoid excessive pressure drop.

3. Numerical model: overview and method of application

3.1. Thermo-fluid dynamic model of microchannel solar receiver

In order to analyse the various proposed compact structures for the pressurised receiver, a bi-dimensional model has been developed, exploiting its implicit simplicity and versatility, permitting different geometries to be easily incorporated and evaluated. The overall structure of the receiver model is portrayed in Figure 5.

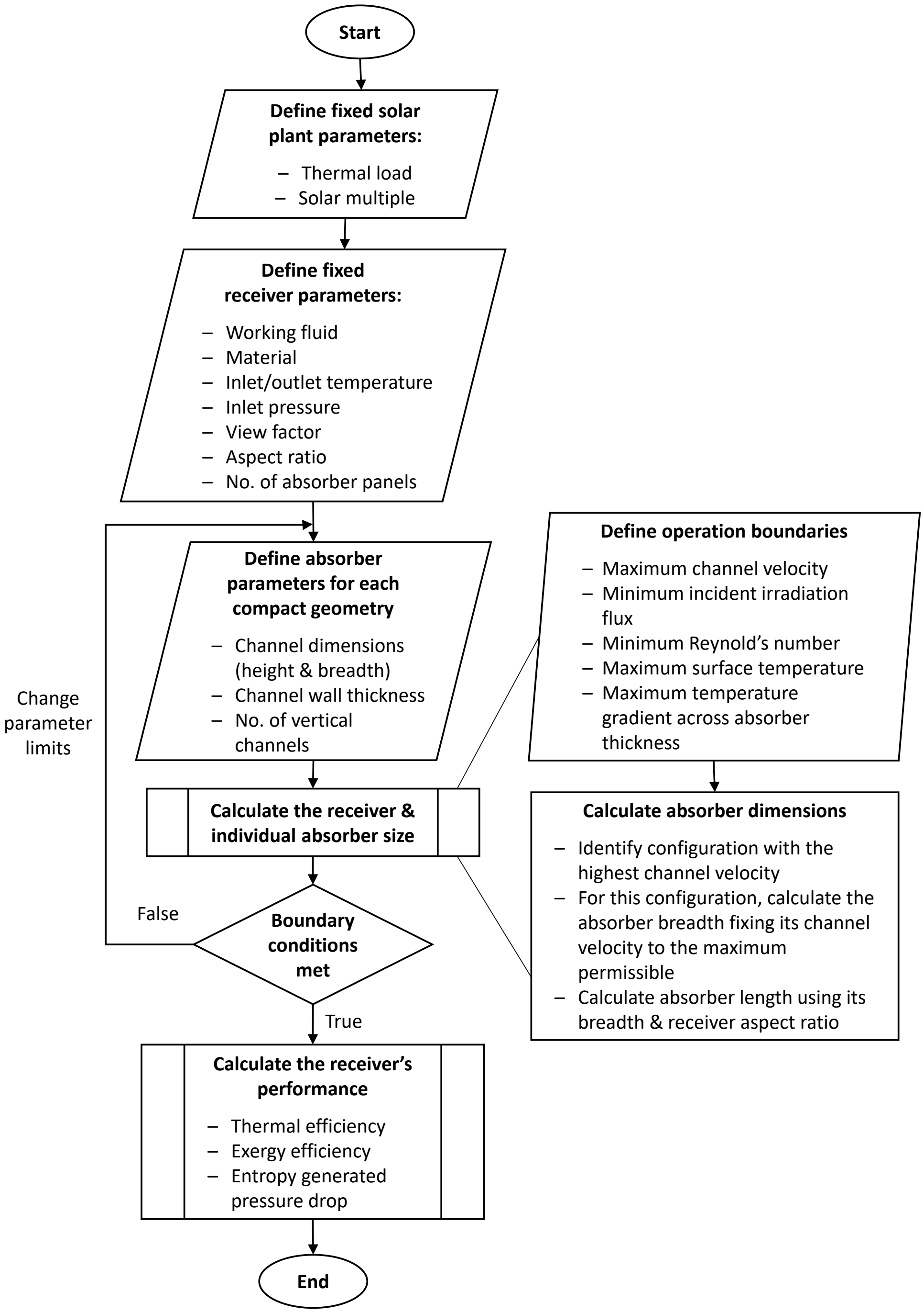

Figure 5. Overall process flow of the pressurised air receiver model.

After determining the global operating conditions of the receiver (Table 2), the analysis of the individual absorber is performed. It is important to note that all absorbers of the receiver are considered to operate under the same conditions and hence only one absorber need be analysed to comprehend the performance of the overall receiver.

The model works by dividing the absorber into multiple elements along its length, each referred to as a Heat Collector Element (HCE). For each HCE, the radial heat flux is initially assumed to be uniform and normal to every surface, and it is evaluated at the average temperature between the inlet and outlet of the HCE. These are conventional assumptions for bi-dimensional solar receiver models [51],[52].

The incident concentrated solar radiation ($\dot{Q}_{solar}$), affected by the solar trap structure, impinges and is absorbed by the absorber panel ($\dot{Q}_{abs}$). Most of this absorbed radiation is transmitted by conduction through the panel walls and the compact structure ($\dot{Q}_{cond,wall}$) to be finally transmitted by convection to the working fluid ($\dot{Q}_{conv,HTF}$). Since the outer wall of the panel is usually at a higher temperature than the ambient, there is a convection and radiation heat loss ($\dot{Q}_{loss,conv}$ and $\dot{Q}_{loss,rad}$, respectively). The total heat loss also includes the contribution due to reflected radiation ($\dot{Q}_{loss,ref}$), which is not absorbed by the panel. The solar trap arrangement seeks to reduce these heat losses. These heat transfer phenomena are summarised in equations (2)-(5):

$$\dot{Q}_{solar} = \dot{Q}_{abs} + \dot{Q}_{loss,ref} \ , \tag{2}$$

$$\dot{Q}_{abs} = \dot{Q}_{cond,wall} + \dot{Q}_{loss,conv} + \dot{Q}_{loss,rad} \ , \tag{3}$$

$$\dot{Q}_{cond,wall} = \dot{Q}_{conv,HTF} \ , \tag{4}$$

$$\dot{Q}_{loss} = \dot{Q}_{loss,conv} + \dot{Q}_{loss,rad} + \dot{Q}_{loss,ref} \ . \tag{5}$$

This system of four equations is completed by a first law energy balance applied to the working fluid, as it passes through each HCE as expressed in equation (6);

$$\dot{Q}_{conv,HTF} = \dot{m}\left[(h_{out} - h_{in}) + \frac{1}{2}\left(v_{out}^2 - v_{in}^2\right)\right] , \tag{6}$$

where $\dot{m}$ is the mass flow rate, h is the enthalpy and v is the fluid velocity. In this equation, potential energy is neglected because, although the receiver is vertical, the height of the absorber panel is short. Additionally, the top row of the absorber panels has a different potential energy change than the bottom row as in one the flow is upwards and in the other downwards. As the model is a simplified amalgamation of all the panels, it was considered unnecessary to do take the negligible, equal and opposite potential energy changes into account. The required HTF thermal properties at the HCE outlet are calculated once the HCE inlet thermal properties and the boundary conditions are known. Of course, the inlet conditions of an element are simply the outlet conditions of the preceding element with the exception of the very first element whose inlet conditions are predefined.

The outlet pressure is determined by calculating the pressure drop across the element and subtracting that from the inlet pressure. With these two properties known, the remaining required fluid properties can be determined. This process is sequentially implemented from the first HCE (at the absorber inlet) to the final HCE (at the absorber outlet). If the HTF outlet temperature is within the tolerance range of the setpoint i.e. 700 °C ± 3 °C, the performance indicators of the absorber (thermal and exergy efficiency, pressure drop, etc.) are evaluated before proceeding to the next absorber configuration. These process steps are schematically outlined in Figure 6. Determination of the heat transfer coefficient and friction factor is required in each HCE and is done by implementing empirical and semi-empirical correlations. These correlations are unique to each CHE geometry and are tabulated in the annexes A.2 and A.3.

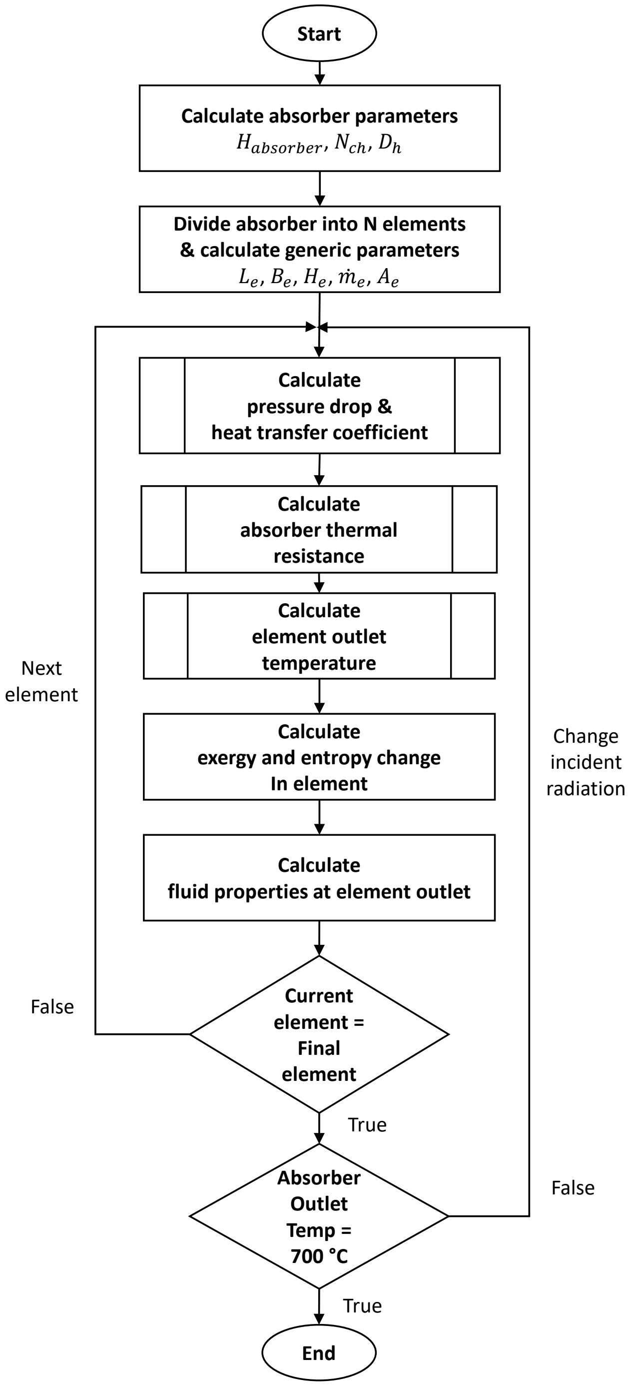

Figure 6. Absorber evaluation subprocess.

As indicated previously, to quantify the external surface heat losses it is first required to determine the absorber's surface temperature. This temperature distribution through the absorber depth (from the irradiated front surface to the back of the absorber) is determined using a Thermal Resistance Model (TRM) accounting for the fluid flow characteristics and the thermal properties of the receiver material [33],[53],[54]. Figure 7 depicts the thermal model for the simplest geometry, plain rectangular fin, but is also indicative of the other geometries.

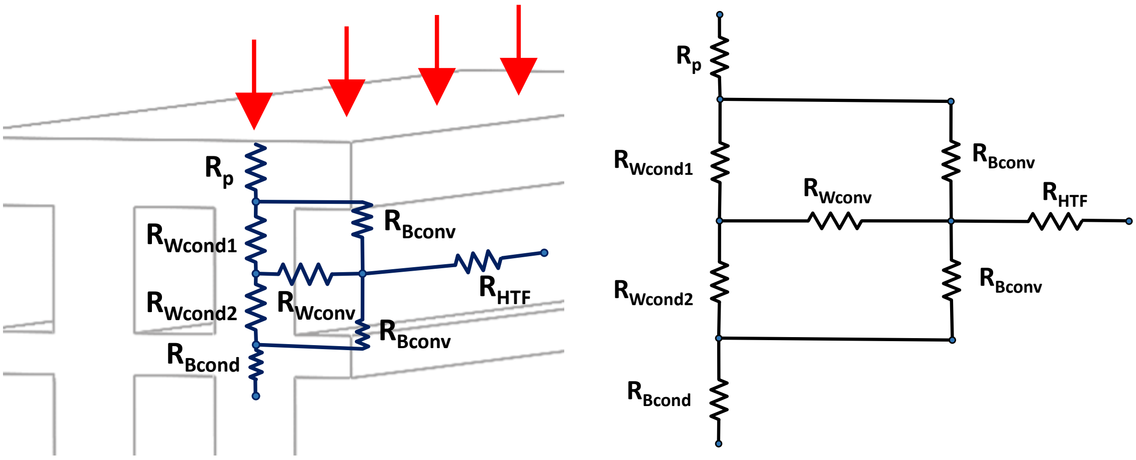

Figure 7. Thermal resistance model in HCE of absorber with plain rectangular fin geometry. Red arrows indicate the irradiated plane and direction of heat transfer.

The equation set to determine the thermal resistance for each HCE is further detailed in equations (7-13). The conductive thermal resistance of the top plate wall (R_p) is defined in equation (7);

$$R_p = \frac{t_p}{k_{absorber} \left(\frac{B_c}{2}\right) L_e} , \tag{7}$$

where t_p is the top plate thickness, $k_{absorber}$ is the thermal conductivity of the absorber and L_e is the length of the HCE. The convective thermal resistance of the channel walls ($R_{w,conv}$) is given in equation (8),

$$R_{w,conv} = \frac{1}{h_{conv} \, H_c \, L_e} , \tag*{8)}$$

where h_{conv} is the heat transfer coefficient. The convective and conductive thermal resistance of the base wall ($R_{b,conv}$ and $R_{b,cond}$) are respectively calculated by equations (9) and (10),

$$R_{b,conv} = \frac{1}{h_{conv} \left(\frac{B_c}{2}\right) L_e} , \tag*{9)}$$

$$R_{b,cond} = \frac{t}{k_{absorber} \left(\frac{B_c + t}{2}\right) L_e} . \tag{10}$$

Equation (11) computes the conductive thermal resistance of the channel half wall ($R_{w,cond}$),

$$R_{w,cond} = \frac{H_c}{2 \, k_{absorber} \left(\frac{t}{2}\right) L_e} . \tag{11}$$

The thermal resistance due to the fluid heat gain (R_{HTF}) is defined in equation (12),

$$R_{HTF} = \frac{1}{\rho\ c_p\ v\ A_c}\ , \tag{12}$$

where ρ is the density, c_p is the specific heat and v is the fluid velocity. Referring to Figure 7, the total thermal resistance of vertically aligned half-channels in a HCE (which can seamlessly extend to describe the thermal resistance of the whole HCE) is expressed in equation (13):

$$R_{absorber} = R_p + N_{cv}\ \Big[R_{b,cond} + \Big\{R_{b,conv} \parallel \Big(R_{w,cond} + \big((R_{w,cond} + R_{b,conv}) \parallel R_{w,conv}\big)\Big)\Big\}\Big]\ . \tag{13}$$

where the parallel symbol (‖) between two terms x and y ($x \parallel y$) notates one-half of the harmonic mean of x and y. As mentioned previously, this thermal resistance model has been developed specifically for the plain rectangular fin geometry, but it is indicative of all the compact structures analysed, if the correlations for convection heat transfer coefficient and friction factor are specified for each of them. These correlations are summarised in the appendix.

3.2. Numerical validation of model

The thermo-fluid dynamic model has been validated by comparison with data from a Resistance Network Model (RNM) and a Computational Fluid Dynamics (CFD) model implemented using the Icepak 4.2 software [54]. The RNM itself was validated using the CFD model and some limited experimentation. It should be noted that the given application of the model used for validation was for heat sinks and not specifically for solar receivers. However, since it uses a single heat flux on one surface and has a multilayer microchannel geometry, it is well suited for application to solar receiver modelling. The model employed for validation was used to simulate the behaviour of a plain rectangular fin receiver with three channels; one horizontal and three verticals. Copper was used as the solid material and a heat flux of 2 W is applied on the top surface. The model used channels of 0.2 mm × 0.8 mm with a channel thickness of 0.2 mm. The overall length, breadth and height were 30 mm, 0.6 mm and 3.2 mm, respectively. Water was used as fluid with flow rates of 2 ml/min, 6 ml/min and 10 ml/min. However, results using a flow rate of 2 ml/min were invalid for the validation given the heat transfer and pressure drop correlations used.

As observed in Figure 8, the temperature rise in the current model matches that predicted by the validation model and the CFD simulation. There is a significant deviation noted at the beginning and end of the receiver which can be attributed to inherent assumptions made in both models. The current model assumes a uniform heat flux distribution whereas the validation model iteratively solves for the heat flux and temperature distribution (finite difference method) keeping the integrated heat flux over the irradiated surface as constant. The receiver outlet temperature, which may be considered one of the most relevant parameters for receiver's performance evaluation, is well predicted by the model with deviations from the CFD tool and validation model less than 2%.

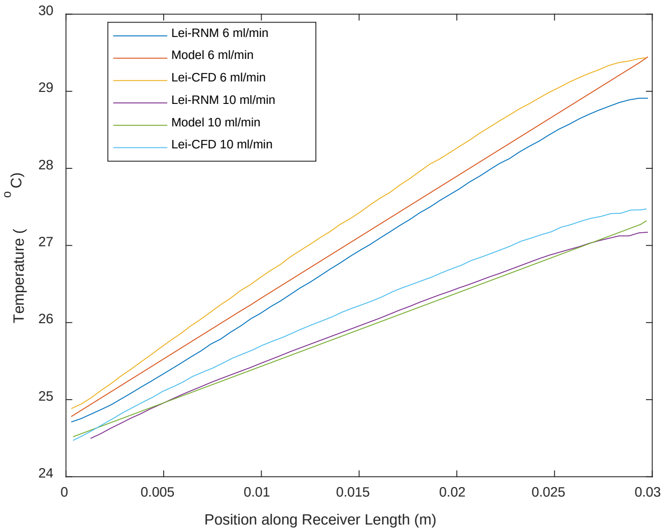

Figure 8. Temperature evolution comparison between model developed in this work and resistance network model and CFD simulations given by Lei [54].

3.3. Performance indicators and objective functions for the parametric analysis

There are several objective functions that can be used when designing and evaluating solar receivers. These include, but are not limited to, exergy efficiency, thermal efficiency, optical efficiency and pressure drops [11]. An exergy analysis is presented with the goal of obtaining a suitable objective function for the receiver optimisation. Such a function must simultaneously account for the useful fluid heat gain and the undesirable heat losses and pressure losses. In conventional heat exchanger theory, functions minimising the entropy rise are widely used [55],[56]. Entropy is generated in the fluid due to the heat gain and also the pressure drop. The general equation quantifying the entropy addition is given by equation (14):

$$\Delta S_{HTF} = \frac{\dot{q}^2_{conv,HTF}}{\pi\, k_{avg}\, T^2_{avg}\, Nu_{avg}} + \frac{32\, \dot{m}^3\, f_D}{\pi^2\, \rho^2_{avg}\, T_{avg}\, D_h^5}\,, \tag{14}$$

which is applied to every HCE. In equation (14), the first term on the right hand side is the contribution made by heat transfer, while the second term is the contribution due to fluid friction; $\dot{q}_{conv_{HTF}}$ is the convection heat transfer per unit length of the HCE; $\dot{m}$ is the mass flow rate per channel, as said before; f_D is the Darcy friction factor; T is the average fluid temperature; ρ is the average fluid density; k is the average fluid conductivity; Nu is the average Nusselt number; and D_h is the hydraulic diameter. Alternatively, exergy gain in the fluid may also be used [57] with the expression for compressible fluids being equation (15)

$$\Delta Ex_{HTF} = \dot{m}\,\left[\Delta h\left(1-\frac{T_{amb}}{T_{LMTD}}\right)+\ R\,T_{amb}\ln\left(\frac{P_{out}}{P_{in}}\right)\right]\ , \tag{15}$$

which is also applied to every HCE; T_{amb} is the ambient temperature; T_{LMTD} is the log mean temperature difference between the HCE outlet and inlet; R is the ideal gas constant; and P is the fluid pressure, evaluated at the inlet and outlet of the HCE. Both equation (14) and (15) have the heat gain term on the left and the pressure drop/fluid friction term on the right. These must be evaluated at the individual HCE level, and then integrated over the absorber length, as the independent variables in these equations change continuously. To factor in the receiver heat losses, the exergy associated to the incident solar radiation is calculated by the Parrot equation (16) [58]:

$$\Delta Ex_{solar} = \dot{Q}_{solar}\ \left[1-\frac{4\,T_{amb}}{3\,T_{sun}}(1-\cos\delta)^{1/4}+\frac{T_{amb}}{3\,T_{sun}}\right]\ , \tag{16}$$

where $\dot{Q}_{solar}$ is the total incident solar radiation on the receiver, also appearing in equation (3); T_{sun} is the equivalent temperature of the sun as a blackbody (~5,800 K); and δ is the half–angle of the cone subtended by the sun's disc ($\delta \sim 4.7$ mrad, on a clear day). Combining equations (15) and (16), a parameter henceforth referred to as the exergy efficiency is obtained as expressed in equation (17);

$$\eta_{exergy} = \frac{\Delta Ex_{HTF}}{\Delta Ex_{solar}}\ . \tag{17}$$

The exergy efficiency, defined in equation (17), factors in all three effects pertinent to the performance of a solar receiver. It can hence act as an objective function to each receiver type, evaluating it for each permutation of the operating parameters, within their ranges, to determine which is the optimum set for each configuration and overall. As mentioned before, there are also other performance indicators that are evaluated and presented including energy efficiency [59], defined in equation (18); and optical efficiency [25], in equation (19);

$$\eta_{energy} = \frac{\dot{Q}_{conv,HTF}}{\dot{Q}_{solar}}\ , \tag{18}$$

$$\eta_{opt} = \frac{\dot{Q}_{abs}}{\dot{Q}_{solar}}\ . \tag{19}$$

4. Results and discussion

4.1. Parametric study

This section presents the results of the parametric study over the range of the four parameters shown in Table 3: channel height (H_c), channel breadth (B_c), number of vertical channels (N_{cv}), and channel thickness (t). It is important to note that only the most relevant and representative figures are selected, given the large scope and quantum of graphical information.

The general expected behaviour and performance of the receiver is first elaborated. Increasing the hydraulic diameter, by increasing the channel height and/or the channel breadth, will reduce the fluid flow velocity in the channels. This will adversely affect the convection coefficient and worsen the heat transfer to the fluid. Consequently, more input heat will be required to achieve the same outlet temperature. The thermal resistance of the absorber will also rise causing higher absorber outer surface temperatures and hence increased thermal losses. On the other hand, the decreased fluid velocity reduces the overall pressure drop in the receiver.

Besides changes to the hydraulic diameter, the fluid velocity is also affected by the number of channels. For a fixed mass flow rate in the receiver, the increase in the number of channels results in decreasing velocity, as the same flow is divided into more channels. The number of horizontal channels is calculated accounting for the fixed absorber breadth and the variable channel breadth and channel wall thickness. An increase in the number of vertical channels hence causes the increase in the thermal resistance by reducing the convective heat transfer coefficient besides by increasing the number of thermal resistances in series in the absorber network. The pressure drop is also expected to decrease with greater channels as it is indirectly related to channel velocity.

Regarding the absorber's equivalent thermal resistance, the channel wall thickness is an important parameter in determining the conductive thermal resistance with thicker walls reducing this resistance and hence allowing for better heat transfer through the solid volume. Thicker walls also reduce the number of horizontal channels and hence, as explained previously, the increase in fluid velocity associated with fewer channels results in higher convection coefficient and lower convective thermal resistance. However, a negative consequence of this effect is that the resulting pressure drop is larger owing to the higher velocities.

As observed in Figure 9, the highest exergy efficiency (58.80%) occurs at the largest channel thickness (t = 3 mm) and smallest number of vertical channels ($N_{cv} = 3$) within the analysed range. The bettering of the heat transfer, with increased channel thickness and reduced vertical channels, clearly outweighs the increased pressure drop, as marked by the rising exergy efficiency. As it will be seen in Figure 10, the rising channel thickness also favoured the energy efficiency.

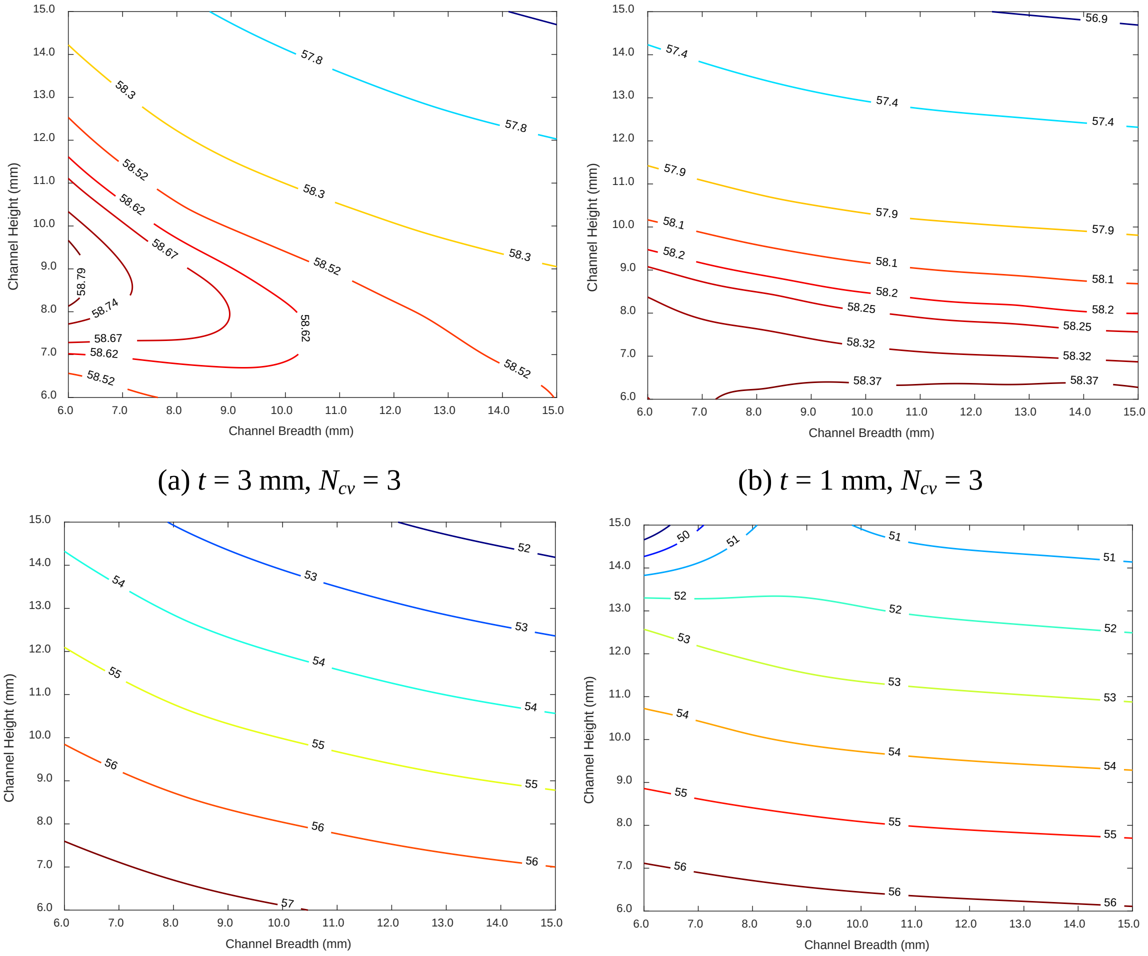

(a) t = 3 mm, N_{cv} = 3 (b) t = 1 mm, N_{cv} = 3

(c) t = 3 mm, N_{cv} = 10 (d) t = 1 mm, N_{cv} = 10

Figure 9. Exergy efficiency (in %) as function of the channel breadth and height for different channel thickness and number of vertical channels for the plain rectangular fin geometry. (a) t = 3 mm, N_{cv} = 3; (b) t = 1 mm, N_{cv} = 3; (c) t = 3 mm, N_{cv} = 10; and (d) t = 1 mm, N_{cv} = 10.

In both Figure 9(a) and Figure 9(b), it is observed that rectangular channels are optimal though with different aspect ratios in each case. This difference in aspect ratios can be attributed to the competing effects of conduction through the solid channel wall and convection to be the preferred mode of heat transfer offering the least thermal resistance. Conduction is favourable when the channel walls are thicker, which leads to the preference for channels with a lower breadth and hence more horizontal channels and channel walls as seen in Figure 9(a). To keep the pressure drop in check, the hydraulic diameter must be sufficiently large which entails a larger channel height to compensate for the optimal channel breadth being at its minimum.

The inverse of this phenomenon is seen in Figure 9(b) when the channel thickness is low and convection offers the less thermally resistive path compared to conduction. Wider channels reduce the number of horizontal channels and channel walls; shorter channels further reduce the solid volume and the related conductive thermal resistance.

When the number of vertical channels is high, as is the case in Figure 9(c) and Figure 9(d), the channel velocities are so low that the pressure drop factor in the efficiency is inconsequential. This is further evidenced by the fact that the corresponding energy efficiency contours i.e Figure 10(c) and Figure 10(d), are identical in trend. The maximum exergy efficiency hence occurs at the smallest channel sizes with the largest channel thickness which together provide the least thermal resistance and best heat transfer to the fluid.

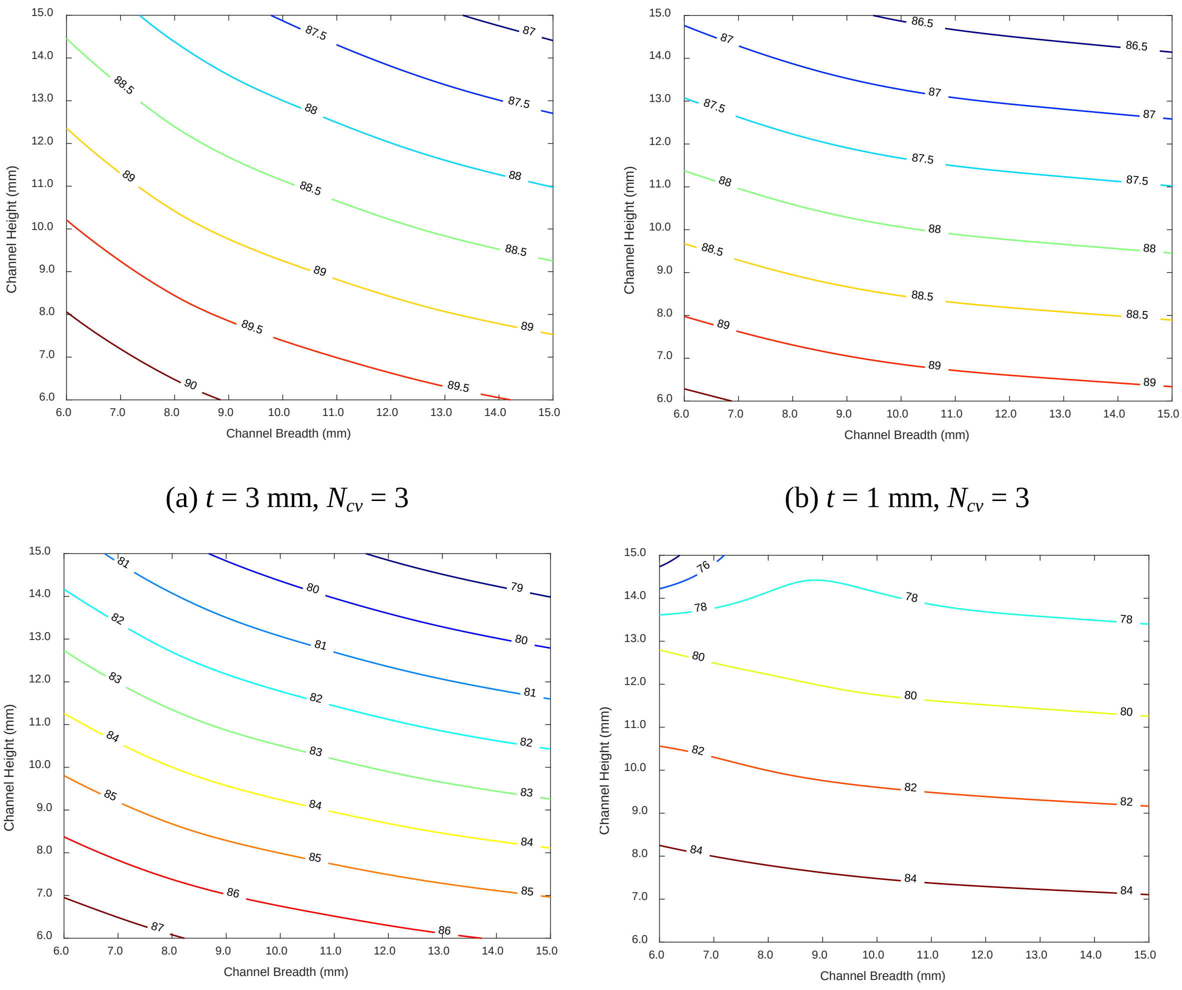

(a) t = 3 mm, N_{cv} = 3 (b) t = 1 mm, N_{cv} = 3

(c) t = 3 mm, N_{cv} = 10 (d) t = 1 mm, N_{cv} = 10

Figure 10. Energy efficiency (in %) as function of the channel breadth and height for different channel thickness and number of vertical channels in the plain rectangular fin geometry. (a) t = 3 mm, N_{cv} = 3; (b) t = 1 mm, N_{cv} = 3; (c) t = 3 mm, N_{cv} = 10; and (d) t = 1 mm, N_{cv} = 10.

In parallel, Figure 10 shows the energy efficiency variation for the same parametric study applied to the plain rectangular fin geometry. From this, it is evident that the behaviour of the energy efficiency is relatively simple as it only considers the heat transfer phenomena and not the related pressure drop. Smaller and fewer channels with thicker walls all work to increase the energy efficiency. These trends hold true for all receiver configurations. On the other hand, the exergy efficiency behaviour in other receiver configurations is more complex as the HTF flow characteristics are significantly different.

Sankey and Grassmann diagrams, shown in Figure 11, help visualise the energetic and exergetic phenomena occurring in the receiver respectively. These diagrams have been generated for the optimum geometrical configuration of the plain rectangular fin receiver, i.e. the parameter set resulting in the maximum exergy efficiency.

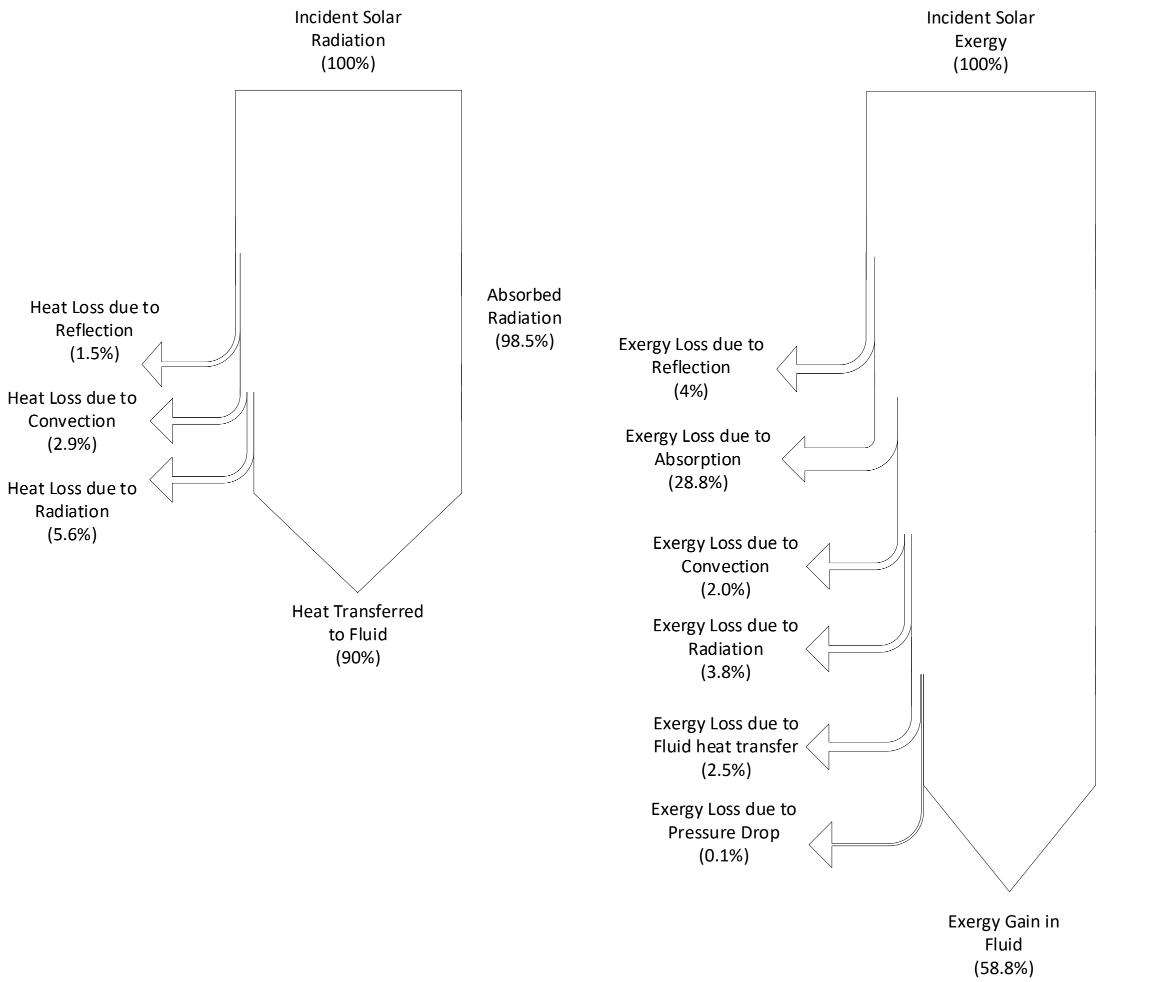

(a) Sankey (energy flow) diagram (b) Grassmann (exergy flow) diagram

Figure 11. Sankey and Grassmann diagram depicting the energy and exergy flow in the plain rectangular fin geometry receiver with the optimum (maximum exergy efficiency) configuration set: H_c = 8.25 mm, t = 3 mm, N_{cv} = 3, B_c = 6 mm

Referring to Figure 11(a), the three energy loss mechanisms, namely reflection, convection and radiation, subtract from incident solar radiation on the receiver as has been described in section 2.4. The final heat transferred to the fluid, after deducting the energy losses, represents the same energy efficiency as described by equation (18). There are more physical phenomena that cause exergy loss in the system, quantified as per standard exergy analyses

[60],[61], as can be seen in Figure 11(b). It is observed that the highest exergy loss is associated with the absorption of the incident solar exergy by the receiver. While the exergy loss related to pressure drop, as a fraction of the solar exergy, is negligible it is nonetheless critical to the performance of the receiver as is clear from Figure (9) and the ensuing discussion. The net exergy gain in the fluid corresponds to the exergy efficiency as defined in equation (17).

4.2. Comparative and optimisation analysis

Using the exergy efficiency as the objective function to be maximised, the different receiver geometries have been optimised (within the operating range of the four varied parameters) for the configuration yielding the highest exergy efficiency. The energy efficiency and the pressure drop corresponding to these configurations have also been tabulated and it can be found in Table 4.

Table 4. Receiver configurations yielding maximum exergy efficiency.

Receiver compact geometry	**(Maximum) exergy efficiency (%)**	**Energy efficiency (%)**	**Pressure drop (bar)**	**Absorber panel dimensions**			
				H_c (mm)	N_{cv} (-)	B_c (mm)	t (mm)
PRF	58.80	89.96	0.35	8.25	3	6.00	3.00
PTF	55.33	85.43	0.55	6.00	5	6.00	3.00
WF	58.37	89.01	0.24	6.00	5	6.00	3.00
OSF	56.09	86.62	0.57	12.75	3	6.00	3.00
PF	59.21	90.14	0.19	6.00	3	6.00	3.00
LF	53.03	81.82	0.53	7.00	3	7.00	1.00

As it can be observed from Table 4, the perforated rectangular fin has the highest exergy efficiency (59.21%), followed by the plain rectangular fin (58.8%) and the wavy fin (58.37%). The corresponding energy efficiency also follows a similar trend (90.14%, 89.96% and 89.01% respectively). Owing to the inherent differences in each geometry's heat transfer and pressure drop characteristics, the resulting optimal configuration for each geometry is different. Simply put, the exergy efficiency is highest when the heat transfer to the fluid is maximal i.e the heat losses are minimal and the pressure drop over the flow length is minimal. These two factors run opposed to one another i.e better fluid heat transfer necessitates greater pressure drop.

In this regard there are interesting trade-offs seen between the number of vertical channels and the channel dimensions, especially its height. This can be clearly visualised in the contour plots of the different geometries at their optimal configurations in Figure 12 which excludes the plain rectangular fin geometry to avoid repeating Figure 9(a).

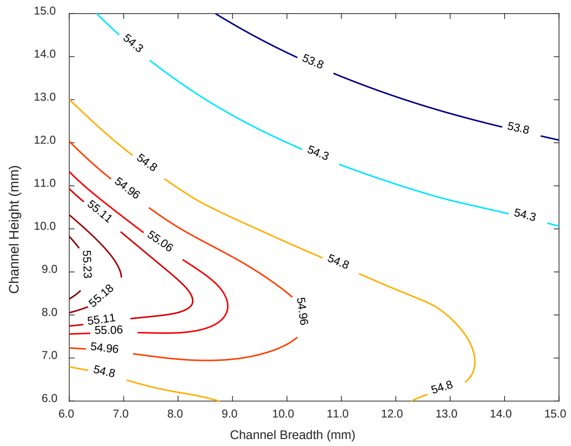

(a) PTF: t = 3 mm, N_{cv} = 3

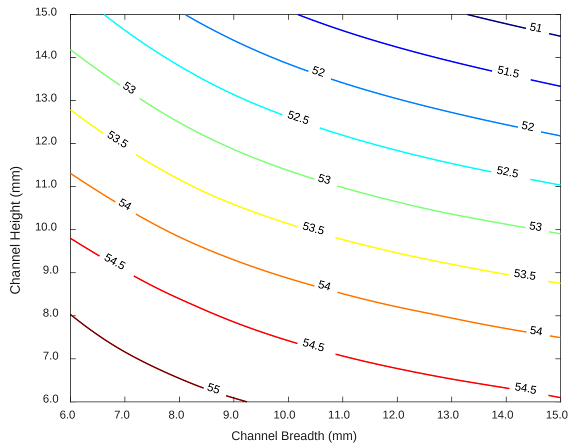

(b) PTF: t = 3 mm, N_{cv} = 5

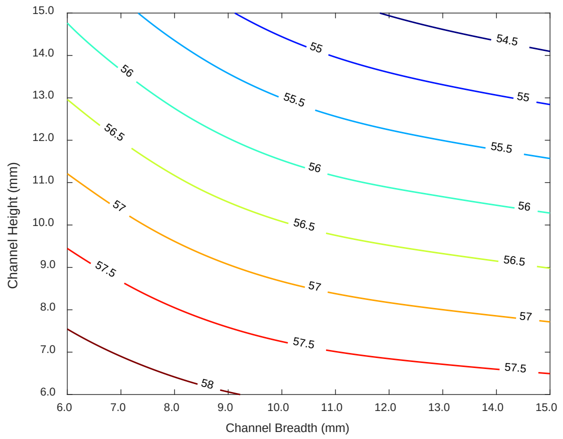

(c) WF: t = 3 mm, N_{cv} = 5

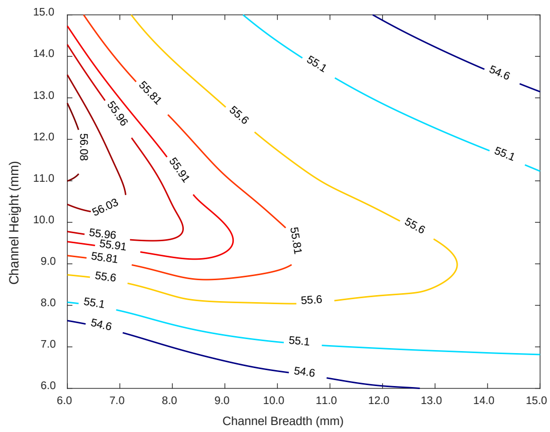

(d) OSF: t = 3 mm, N_{cv} = 3

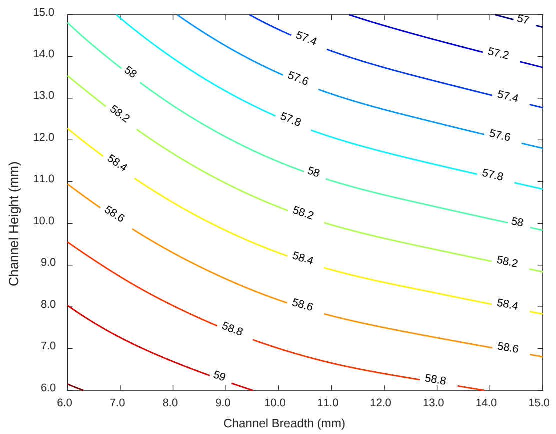

(e) PF: t = 3 mm, N_{cv} = 3

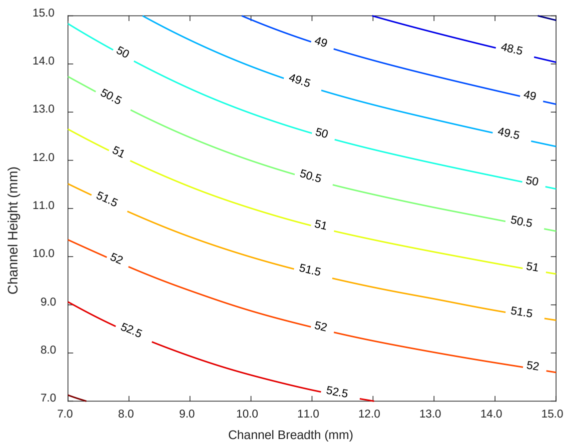

(f) LF: t = 1 mm, N_{cv} = 3

Figure 12. Exergy efficiency as function of the channel breadth and height, for different absorber geometries. (a) PTF: t = 3 mm, N_{cv} = 3; (b) PTF: t = 3 mm, N_{cv} = 5; (c) WF: t = 3 mm, N_{cv} = 5; (d) OSF: t = 3 mm, N_{cv} = 3; (e) PF: t = 3 mm, N_{cv} = 3; (f) LF: t = 1 mm, N_{cv} = 3.

Comparing the plain triangular fin geometry's optimal configuration in Figure 12(b) with its performance using fewer vertical channels in Figure 12(a), it can be seen that the trends in both ultimately serve to reduce the pressure drop though in different ways. By either increasing the number of channels, as is the case with the wavy fin in addition to the plain triangular fin, or the hydraulic diameter, which is the case with the plain rectangular and offset strip fin, this purpose may be sufficiently served.

In the case of the perforated fin, the pressure drop is sufficiently low to allow for the configuration with, theoretically, the greatest pressure drop to coincide with the optimal exergy efficiency operation point. The louvred fin geometry has the interesting feature of combining higher convective heat transfer with greater pressure loss and this is what leads to its optimal configuration having the smallest channel thickness. However, this excessive pressure loss causes it to have the worst exergy efficiency.

It should be noted though that the relative differences between the various CHE optimal configurations (especially the aforementioned top three performers) are not large and may fall within the range of modelling uncertainty. In this regard, the correlations in the appendix already have uncertainties in the range of 3-10%. While the precise values of these performance indicators may be further refined and their errors ascertained, these results provide a good indication of the relative performances of the different receiver internal flow geometries. They also highlight the immense scope of work in this area and the importance of a thorough and careful optimisation analysis paying heed to the selection of objective functions and figures of merit.

5. Conclusions and future work

Compact heat exchangers are a commercially demonstrated technology that improves the heat transfer and the volumetric efficiency of heat exchange devices. Such compact heat exchangers come in many geometrical forms, when it comes to the internal channels or flow paths, each with their unique properties. The application of these concepts to solar towers results in microchannel receivers that show the potential of operating at high temperatures while maintaining high reliability and thermal efficiency. This is especially true when the heat transfer fluid employed is a pressurised gas, as smaller channels are thermo-mechanically more capable of handling such fluids. In this context, this study has investigated the use of different receiver internal flow geometries, inspired by compact heat exchanger concepts, to analyse the performance of various microchannel receivers. It has been assumed that the heat transfer fluid through the receiver is pressurised air. In this analysis, the particular conditions at the receiver inlet/outlet are determined by coupling the receiver to a supercritical CO_2 recompression cycle, although other coupling possibilities would also be valid.

For this microchannel receiver, the compact geometries analysed were the plain rectangular fin, plain triangular fin, perforated fin, wavy fin, offset strip fin and the louvred fin. Besides comparing several compact geometries, internal parametric and optimisation studies were performed with each flow geometry to determine the optimum configuration. The parameters varied were the channel height, breadth, wall thickness (between channels) and the number of vertical channels (number of channels along the height dimension).

Exergy efficiency has been defined and identified as a suitable performance indicator and objective function to be maximised for the optimisation study. It is deemed suitable as it accounts for the heat losses besides the heat transferred to the fluid and the pressure drop across the receiver. Perforated fin followed by plain rectangular and wavy fin receivers were identified as the best performing receiver subtypes.

The thermal resistance of the receiver, in addition to the pressure drop, plays an important role in determining the optimal geometric configuration. For the best heat transfer to the fluid, which is an important part of the exergy efficiency, the smallest channels or lowest hydraulic diameters are preferred. If this causes excessive pressure drops, either deeper channels or a greater number of vertical channels is preferred to improve the exergy efficiency by mitigating the pressure drop. In virtually all cases narrower channels with thicker walls are favoured because of the better conduction through the solid receiver channel walls compared to the parallel heat flow path of convection via the pressurised air. The lower thermal resistance lowers the receiver's heat loss, as well as provides a more uniform temperature through the receiver.

The methodology used in the analysis, its inherent assumptions in addition to the operating and boundary conditions and limits, lends itself to the characteristics of gas phase receivers and the unique challenges posed in studying such receivers. The selection of operating and boundary conditions including, but not limited to, parameters such as the channel velocity, view factor and incident flux play an important part in the receiver's performance and optimal configuration. Investigating the physical limits and phenomena limiting the operation boundary of gas receivers, aside from developing methodologies for their analysis, appears as an interesting area of study.

The present results indicate a promising scope to the use of compact heat exchanger concepts for solar receivers especially with regards the internal flow channel geometry. While the results themselves carry some uncertainties (an area of future investigation), this analysis clearly demonstrates the utility of using exergy efficiency as a performance indicator and it provides indications to the comparative performance of different receiver geometry types. A regression analysis and modelling for each geometry is proposed to allow for further analysis and its easier coupling in other studies including overall cycle analyses. More work is required to more accurately model the thermo-physical processes occurring in such microchannel receivers. 3D Computational Fluid Dynamics (CFD) models and experimental demonstrations of these microchannel receivers are also required to validate these findings.

Acknowledgments

This work has been developed within the framework of the ACES2030-CM project, funded by the Regional Research and Development in Technology Programme 2018 (ref. P2018/EMT-4319). The authors would like to thank the support of the Spanish Ministry of Economy and Competitiveness through the PID2019-110283RB-C31 project.

References

[1] IRENA, Renewable Power Generation Costs in 2020, International Renewable Energy Agency, Abu Dhabi, 2021.

[2] Sunshot, SunShot Vision Study, Solar Energy Technologies Office, 2012.

[3] M. Mehos, C. Turchi, J. Vidal, M. Wagner, Z. Ma, Concentrating Solar Power Gen3 Demonstration Roadmap, Renew. Energy. (2017) 140.

[4] W. Wang, B. Laumert, Effect of cavity surface material on the concentrated solar flux distribution for an impinging receiver, Sol. Energy Mater. Sol. Cells. 161 (2017) 177–182. https://doi.org/10.1016/j.solmat.2016.12.008.

[5] C.S. Turchi, J. Vidal, M. Bauer, Molten salt power towers operating at 600–650 °C: Salt selection and cost benefits, Sol. Energy. 164 (2018) 38–46. https://doi.org/10.1016/j.solener.2018.01.063.

[6] T. Neises, C. Turchi, Supercritical carbon dioxide power cycle design and configuration optimization to minimize levelized cost of energy of molten salt power towers operating at 650 °C, Sol. Energy. 181 (2019) 27–36. https://doi.org/10.1016/j.solener.2019.01.078.

[7] S. Bell, T. Steinberg, G. Will, Corrosion mechanisms in molten salt thermal energy storage for concentrating solar power, Renew. Sustain. Energy Rev. 114 (2019) 109328. https://doi.org/10.1016/j.rser.2019.109328.

[8] C.K. Ho, B.D. Iverson, Review of high-temperature central receiver designs for concentrating solar power, Renew. Sustain. Energy Rev. 29 (2014) 835–846. https://doi.org/10.1016/j.rser.2013.08.099.

[9] C.K. Ho, J.D. Ortega, J.M. Christian, J.E. Yellowhair, D.A. Ray, J.W. Kelton, G. Peacock, C.E. Andraka, S. Shinde, Fractal-Like Materials Design with Optimized Radiative Properties for High-Efficiency Solar Energy Conversion, 2016. https://doi.org/10.2172/1431480.

[10] C.K. Ho, Advances in central receivers for concentrating solar applications, Sol. Energy. 152 (2017) 38–56. https://doi.org/10.1016/j.solener.2017.03.048.

[11] M. Sedighi, R. Vasquez Padilla, M. Lake, A. Rose, Y.Y. Lim, J.P. Novak, R.A. Taylor, Design of high-temperature atmospheric and pressurised gas-phase solar receivers: A

comprehensive review on numerical modelling and performance parameters, Sol. Energy. 201 (2020) 701–723. https://doi.org/10.1016/j.solener.2020.03.025.

[12] A.L. Ávila-Marín, Volumetric receivers in Solar Thermal Power Plants with Central Receiver System technology: A review, Sol. Energy. 85 (2011) 891–910. https://doi.org/10.1016/j.solener.2011.02.002.

[13] F. Gomez-Garcia, J. González-Aguilar, G. Olalde, M. Romero, Thermal and hydrodynamic behavior of ceramic volumetric absorbers for central receiver solar power plants: A review, Renew. Sustain. Energy Rev. 57 (2016) 648–658. https://doi.org/10.1016/j.rser.2015.12.106.

[14] R. Capuano, T. Fend, P. Schwarzbözl, O. Smirnova, H. Stadler, B. Hoffschmidt, R. Pitz-Paal, Numerical models of advanced ceramic absorbers for volumetric solar receivers, Renew. Sustain. Energy Rev. 58 (2016) 656–665. https://doi.org/10.1016/j.rser.2015.12.068.

[15] E. Almatrafi, A. Khaliq, T. Alquthami, Thermodynamic investigation of a novel cooling-power cogeneration system driven by solar energy, Int. J. Refrig. 138 (2022) 244–258. https://doi.org/10.1016/j.ijrefrig.2022.03.017.

[16] M. Sedighi, R.V. Padilla, R.A. Taylor, M. Lake, I. Izadgoshasb, A. Rose, High-temperature, point-focus, pressurised gas-phase solar receivers: A comprehensive review, Energy Convers. Manag. 185 (2019) 678–717. https://doi.org/10.1016/j.enconman.2019.02.020.

[17] J.D. Ortega, J.M. Christian, C.K. Ho, Design and Testing of a Novel Bladed Receiver, (2017) 9.

[18] European Commission, SOLHYCO (Solar-Hybrid Power and Cogeneration Plants), 2011.

[19] R. Korzynietz, J.A. Brioso, A. del Río, M. Quero, M. Gallas, R. Uhlig, M. Ebert, R. Buck, D. Teraji, Solugas – Comprehensive analysis of the solar hybrid Brayton plant, Sol. Energy. 135 (2016) 578–589. https://doi.org/10.1016/j.solener.2016.06.020.

[20] H.-S. Cho, H.-J. Lee, J.-K. Kim, S.-N. Lee, Y.-H. Kang, Design and Performance Evaluation of Solar Air Receivers, J. Korean Sol. Energy Soc. 32 (2012) 207–212. https://doi.org/10.7836/kses.2012.32.spc3.207.

[21] W. Wang, H. Xu, B. Laumert, T. Strand, An inverse design method for a cavity receiver used in solar dish Brayton system, Sol. Energy. 110 (2014) 745–755. https://doi.org/10.1016/j.solener.2014.10.019.

[22] W. Wang, B. Laumert, H. Xu, T. Strand, Conjugate heat transfer analysis of an impinging receiver design for a dish-Brayton system, Sol. Energy. 119 (2015) 298–309. https://doi.org/10.1016/j.solener.2015.07.013.

[23] W. Wang, B. Wang, L. Li, B. Laumert, T. Strand, The effect of the cooling nozzle arrangement to the thermal performance of a solar impinging receiver, Sol. Energy. 131 (2016) 222–234. https://doi.org/10.1016/j.solener.2016.02.052.

[24] I. Hischier, D. Hess, W. Lipiński, M. Modest, A. Steinfeld, Heat Transfer Analysis of a Novel Pressurized Air Receiver for Concentrated Solar Power via Combined Cycles, J. Therm. Sci. Eng. Appl. 1 (2009) 041002. https://doi.org/10.1115/1.4001259.

[25] I. Hischier, P. Leumann, A. Steinfeld, Experimental and Numerical Analyses of a Pressurized Air Receiver for Solar-Driven Gas Turbines, J. Sol. Energy Eng. 134 (2012) 021003. https://doi.org/10.1115/1.4005446.

[26] P. Poživil, N. Ettlin, F. Stucker, A. Steinfeld, Modular Design and Experimental Testing of a 50 kWth Pressurized-Air Solar Receiver for Gas Turbines, J. Sol. Energy Eng. 137 (2015) 031002. https://doi.org/10.1115/1.4028918.

[27] Q. Li, G. Flamant, X. Yuan, P. Neveu, L. Luo, Compact heat exchangers: A review and future applications for a new generation of high temperature solar receivers, Renew. Sustain. Energy Rev. 15 (2011) 4855–4875. https://doi.org/10.1016/j.rser.2011.07.066.

[28] Q. Li, N.G. de Tourville, I. Yadroitsev, X. Yuan, G. Flamant, Micro-channel pressurized-air solar receiver based on compact heat exchanger concept, Sol. Energy. 91 (2013) 186–195. https://doi.org/10.1016/j.solener.2013.02.004.

[29] W.M. Kays, A.L. London, Compact heat exchangers, (1984). https://www.osti.gov/biblio/6132549 (accessed June 29, 2021).

[30] F. Rajaee, A. Kasaeian, M.A. Vaziri Rad, K. Aliyon, Energetic and exergetic evaluation of a photovoltaic thermal module cooled by hybrid nanofluids in the microchannel, Sol. Energy Adv. 1 (2021) 100005. https://doi.org/10.1016/j.seja.2021.100005.

[31] S. Mukherjee, P.C. Mishra, P. Chaudhuri, Energy and Exergy Viability Analysis of Nanofluids As A Coolant for Microchannel Heat Sink, Int. J. Automot. Mech. Eng. 16 (2019) 6090–6107. https://doi.org/10.15282/ijame.16.1.2019.2.0464.

[32] S.M. Besarati, D. Yogi Goswami, Analysis of Advanced Supercritical Carbon Dioxide Power Cycles With a Bottoming Cycle for Concentrating Solar Power Applications, J. Sol. Energy Eng. 136 (2014) 010904. https://doi.org/10.1115/1.4025700.

[33] S.M. Besarati, D. Yogi Goswami, E.K. Stefanakos, Development of a Solar Receiver Based on Compact Heat Exchanger Technology for Supercritical Carbon Dioxide Power Cycles, J. Sol. Energy Eng. 137 (2015) 031018. https://doi.org/10.1115/1.4029861.

[34] S.M. Besarati, D.Y. Goswami, Supercritical CO2 and other advanced power cycles for concentrating solar thermal (CST) systems, in: Adv. Conc. Sol. Therm. Res. Technol., Elsevier, 2017: pp. 157–178. https://doi.org/10.1016/B978-0-08-100516-3.00008-3.

[35] K. Drost, High Flux Microchannel Receiver Development with Adap-tive Flow Control, 2015. https://doi.org/10.2172/1347906.

[36] T. L'Estrange, Title: Experimental Characterization of a Supercritical Carbon Dioxide Microchannel Solar Thermal Receiver, Oregon State, 2015.

[37] S. Sullivan, High-Efficiency Low-Cost Solar Receiver for use in a Supercritical CO2 Recompression Cycle Brayton, Brayton Energy, LLC, Portsmouth, NH 03842, 2016.

[38] Z.I. Abdulrazzaq ALhsani, R.K. Aldulaimi, Experimental Analysis of Solar Dish Concentrators With Cylindrical, Oval, and Conical Cavity Receivers, Int. J. Renew. Energy Res. (2020). https://doi.org/10.20508/ijrer.v10i2.10594.g7928.

[39] R. Loni, A.B. Kasaeian, E. Askari Asli-Ardeh, B. Ghobadian, S. Gorjian, Experimental and numerical study on dish concentrator with cubical and cylindrical cavity receivers using thermal oil, Energy. 154 (2018) 168–181. https://doi.org/10.1016/j.energy.2018.04.102.

[40] R. Loni, E. Askari Asli-Areh, B. Ghobadian, A.B. Kasaeian, Sh. Gorjian, G. Najafi, E. Bellos, Research and review study of solar dish concentrators with different nanofluids and different shapes of cavity receiver: Experimental tests, Renew. Energy. 145 (2020) 783–804. https://doi.org/10.1016/j.renene.2019.06.056.

[41] S. Sasidharan, P. Dutta, Numerical and experimental studies on a pressurized hybrid tubular and cavity solar air receiver using a Scheffler reflector, Appl. Therm. Eng. 214 (2022) 118898. https://doi.org/10.1016/j.applthermaleng.2022.118898.

[42] M.J. Montes, J.I. Linares, R. Barbero, A. Rovira, Proposal of a new design of source heat exchanger for the technical feasibility of solar thermal plants coupled to supercritical power cycles, Sol. Energy. 211 (2020) 1027–1041. https://doi.org/10.1016/j.solener.2020.10.042.

[43] M. Huber, A. Harvey, E. Lemmon, G. Hardin, I. Bell, M. McLinden, NIST Reference Fluid Thermodynamic and Transport Properties Database (REFPROP) Version 10 - SRD 23, (2018). https://doi.org/10.18434/T4/1502528.

[44] H.E. McCoy, J.F. King, Mechanical properties of Inconel 617 and 618, 1985. https://doi.org/10.2172/711763.

[45] K. Venkatesan, A.T. Mathew, S. Devendiran, N.M. Ghazaly, S. Sanjith, R. Raghul, Machinability study and multi-response optimization of cutting force, Surface roughness and tool wear on CNC turned Inconel 617 superalloy using Al2O3 Nanofluids in Coconut oil, Procedia Manuf. 30 (2019) 396–403. https://doi.org/10.1016/j.promfg.2019.02.055.

[46] P. Falcone, A handbook for solar central receiver design, 1986. https://doi.org/10.2172/6545992.

[47] J.S.M. Jebamalai, Receiver Design Methodology for Solar Tower Power Plants, KTH University, 2016.

[48] J. Yellowhair, C.K. Ho, J.D. Ortega, J.M. Christian, C.E. Andraka, Testing and optical modeling of novel concentrating solar receiver geometries to increase light trapping and

effective solar absorptance, in: A.P. Plesniak, A.J. Prescod (Eds.), San Diego, California, United States, 2015: p. 95590A. https://doi.org/10.1117/12.2186647.

[49] J.R. Howell, M.P. Mengüç, K.J. Daun, R. Siegel, Thermal radiation heat transfer, Seventh edition, CRC Press, Boca Raton, 2021.

[50] J.E. Hesselgreaves, R. Law, D. Reay, Compact Heat Exchangers: Selection, Design and Operation, Butterworth-Heinemann, 2016.

[51] R. Forristall, Heat Transfer Analysis and Modeling of a Parabolic Trough Solar Receiver Implemented in Engineering Equation Solver, 2003. https://doi.org/10.2172/15004820.

[52] M.J. Montes, R. Barbero, R. Abbas, A. Rovira, Performance model and thermal comparison of different alternatives for the Fresnel single-tube receiver, Appl. Therm. Eng. 104 (2016) 162–175. https://doi.org/10.1016/j.applthermaleng.2016.05.015.

[53] Xiaojin Wei, Y. Joshi, Optimization study of stacked micro-channel heat sinks for micro-electronic cooling, IEEE Trans. Compon. Packag. Technol. 26 (2003) 55–61. https://doi.org/10.1109/TCAPT.2003.811473.

[54] N. Lei, The Thermal Characteristics Of Multilayer Minichannel Heat Sinks In Single-Phase And Two-Phase Flow, Doctoral, University of Arizona, 2006.

[55] A. Bejan, The thermodynamic design of heat and mass transfer processes and devices, Int. J. Heat Fluid Flow. 8 (1987) 258–276. https://doi.org/10.1016/0142-727X(87)90062-2.

[56] A. Bejan, Entropy generation minimization: The new thermodynamics of finite-size devices and finite-time processes, J. Appl. Phys. 79 (1996) 1191–1218. https://doi.org/10.1063/1.362674.

[57] S.A. Ashrafizadeh, Application of Second Law Analysis in Heat Exchanger Systems, Entropy. 21 (2019) 606. https://doi.org/10.3390/e21060606.

[58] J.E. Parrott, Theoretical upper limit to the conversion efficiency of solar energy, Sol. Energy. 21 (1978) 227–229. https://doi.org/10.1016/0038-092X(78)90025-7.

[59] J.P. Holman, Heat transfer, 10th ed, McGraw Hill Higher Education, Boston, 2010.

[60] K. Altfeld, W. Leiner, M. Fiebig, Second law optimization of flat-plate solar air heaters Part I: The concept of net exergy flow and the modeling of solar air heaters, Sol. Energy. 41 (1988) 127–132. https://doi.org/10.1016/0038-092X(88)90128-4.

[61] M.K. Sahu, R.K. Prasad, Exergy based performance evaluation of solar air heater with arc-shaped wire roughened absorber plate, Renew. Energy. 96 (2016) 233–243. https://doi.org/10.1016/j.renene.2016.04.083.

[62] S.S. Mehendale, A.M. Jacobi, R.K. Shah, Fluid Flow and Heat Transfer at Micro- and Meso-Scales With Application to Heat Exchanger Design, Appl. Mech. Rev. 53 (2000) 175–193. https://doi.org/10.1115/1.3097347.

[63] S. Kakaç, H. Liu, A. Pramuanjaroenkij, Heat Exchangers: Selection, Rating, and Thermal Design, Third Edition., CRC Press, Hoboken, 2012.

[64] L. Sheik Ismail, R. Velraj, C. Ranganayakulu, Studies on pumping power in terms of pressure drop and heat transfer characteristics of compact plate-fin heat exchangers—A review, Renew. Sustain. Energy Rev. 14 (2010) 478–485. https://doi.org/10.1016/j.rser.2009.06.033.

[65] K.W. M, L.A. L, Compact Heat Exchangers (3rd Edition), 2018. https://app.knovel.com/hotlink/toc/id:kpCHEE0002/compact-heat-exchangers (accessed August 16, 2021).

[66] X. Sun, X. Zhang, R. Christensen, M. Anderson, Compact Heat Exchanger Design and Testing for Advanced Reactors and Advanced Power Cycles, 2018. https://doi.org/10.2172/1437159.

[67] A. Katz, S.R. Aakre, M.H. Anderson, D. Ranjan, Experimental investigation of pressure drop and heat transfer in high temperature supercritical CO2 and helium in a printed-circuit heat exchanger, Int. J. Heat Mass Transf. 171 (2021) 121089. https://doi.org/10.1016/j.ijheatmasstransfer.2021.121089.

[68] P.S. McNeff, B.K. Paul, Manufacturing Process Design of a Microchannel Solar Receiver using Electrically-Assisted Embossing, Procedia Manuf. 48 (2020) 187–196. https://doi.org/10.1016/j.promfg.2020.05.037.

[69] N.A.A. Qasem, S.M. Zubair, Compact and microchannel heat exchangers: A comprehensive review of air-side friction factor and heat transfer correlations, Energy Convers. Manag. 173 (2018) 555–601. https://doi.org/10.1016/j.enconman.2018.06.104.

[70] A. Diani, S. Mancin, C. Zilio, L. Rossetto, Experimental and numerical analyses of different extended surfaces, J. Phys. Conf. Ser. 395 (2012) 012045. https://doi.org/10.1088/1742-6596/395/1/012045.

[71] M.V.V. Mortean, M.B.H. Mantelli, Nusselt number correlation for compact heat exchangers in transition regimes, Appl. Therm. Eng. 151 (2019) 514–522. https://doi.org/10.1016/j.applthermaleng.2019.02.017.

[72] V. Gnielinski, New equations for heat and mass transfer in turbulent pipe and channel flow, Int. Chem. Eng. 16 (1976) 359–368.

[73] M. Khoshvaght Aliabadi, F. Hormozi, E. Hosseini Rad, New correlations for wavy plate-fin heat exchangers: different working fluids, Int. J. Numer. Methods Heat Fluid Flow. 24 (2014) 1086–1108. https://doi.org/10.1108/HFF-09-2012-0195.

[74] S. Mochizuki, Y. Yagi, W.-J. Yang, Transport Phenomena in Stacks of Interrupted Parallel-Plate Surfaces, Exp. Heat Transf. 1 (1987) 127–140. https://doi.org/10.1080/08916158708946336.

[75] J. Deng, Improved correlations of the thermal-hydraulic performance of large size multi-louvered fin arrays for condensers of high power electronic component cooling by

numerical simulation, Energy Convers. Manag. 153 (2017) 504–514. https://doi.org/10.1016/j.enconman.2017.09.066.

[76] M.R. Shaeri, M. Yaghoubi, K. Jafarpur, Heat transfer analysis of lateral perforated fin heat sinks, Appl. Energy. 86 (2009) 2019–2029. https://doi.org/10.1016/j.apenergy.2008.12.029.

[77] T.K. Ibrahim, A.T. Al-Sammarraie, M.S.M. Al-Jethelah, W.H. Al-Doori, M.R. Salimpour, H. Tao, The impact of square shape perforations on the enhanced heat transfer from fins: Experimental and numerical study, Int. J. Therm. Sci. 149 (2020) 106144. https://doi.org/10.1016/j.ijthermalsci.2019.106144.

[78] A. Diani, S. Mancin, C. Zilio, L. Rossetto, An assessment on air forced convection on extended surfaces: Experimental results and numerical modeling, Int. J. Therm. Sci. 67 (2013) 120–134. https://doi.org/10.1016/j.ijthermalsci.2012.11.012.

Appendix

A. 1. Compact heat exchanger type structures applied to central solar receivers

There is no single definition of a Compact Heat Exchanger (CHE) although it is usually thought of as a Heat Exchanger (HX) having a surface area density above 700 m^2/m^3 or a hydraulic diameter below 6 mm, if at least one fluid is a gas [27],[62],[63]. The reduction in hydraulic diameter leads to the following outcomes:

- A reduction in the solid volume required for the same effective heat transfer area potentially resulting in significant savings in material costs [64].
- A higher heat transfer coefficient, due to decreased diffusion length compared to conventional channels or tubes, as mentioned before [65].
- The main drawback of this concept which is that pressure drop increases, although this effect may be offset if the gas is pressurised, as velocity is much lower at high pressure, for the same mass flow and same cross section, as explained in the previous section.

There have been several studies investigating the use of CHEs as the intermediary HX between the solar field and the power block [42],[66],[67]. but fewer studies into directly using CHE geometries and concepts for solar receivers, as summarised in the next paragraphs.

The operational limits of the main types of CHEs are presented in **Table A.1**, although it should be noted that these limits are not absolute and largely depend on the materials used and manufacturing processes. It is intended to be indicative of the relative capacities of each type of CHE.

Table A.1. Operational limits of CHEs. PHE represents Plate Heat Exchanger; PFHE stands for Plate Fin Heat Exchanger; PCHE denotes Printed Circuit Heat Exchanger; and SHE denotes Spiral Heat Exchanger. [27]

CHE Type	Maximum temperature (°C)	Maximum pressure (bar)
Gasketed PHE	200-250	35
Brazed PHE	225	45
PFHE	800	120
Diffusion bonded PFHE	800	620
PCHE	900	500-1,000
SHE	540	25

Given the high temperature requirements of all solar receivers (> 900 °C), Plate Heat Exchangers (PHEs) are not feasible and the CHEs must use materials that can withstand such temperatures such as ceramics, nickel and titanium alloys. Diffusion bonded Plate Fin Heat Exchangers (PFHEs) and Printed Circuit Heat Exchangers (PCHEs) were considered the most suitable candidates for application as solar receivers, due to their high efficiency as well as mechanical strength. Nevertheless, for typical PGR working pressures, even in the case of direct coupling with a supercritical power cycle (approximately 200 bar), it is sufficient to use a diffusion bonded PFHE type, so the research has focused on this type, yielding to several prototypes described in next section.

Finally, it is interesting to note that there are additive methods to manufacture these compact structures including Electrically Assisted (EA) forming [68] and Selective Laser Melting (SLM) [28] that provide a greater degree of flexibility in the design of the CHE microchannels There are also novel techniques, specifically Electrical Discharge Machining (EDM), employed to increase the aspect ratio (channel height to width) in PFHEs [35],[36].

A. 2. Heat transfer correlations (channel flow)

Heat transfer correlations, in terms of Colburn factor (j) or Nusselt Number (Nu), are presented in Table A.2, for the different compact geometries analysed in this work, at different operating conditions.

Table A.2. Heat transfer correlations, in terms of Colburn factor (j) or Nusselt Number (Nu) for the different compact geometries analysed

Receiver	Validity	Correlation	Reference
Plain Rectangular Fin	$2700 < Re_{D_h} < 10100$	$j = 0.609\, Re_{D_h}^{-0.493} \left(\frac{t}{H_c}\right)^{-0.011} \left(\frac{p}{H_c}\right)^{-0.071} \left(\frac{L_e}{D_h}\right)^{-0.298}$	[69],[70]
	$Re_{D_h} > 10100$ $0.5 < Pr_{D_h} < 2000$	$Nu_{D_h} = \frac{f_D}{2}\left(Re_{D_h} - 1000\right) Pr_{D_h} \left(1 + 12.7\left(\frac{f_D}{2}\right)^{0.5}\left(Pr_{D_h}^{\frac{2}{3}} - 1\right)\right)^{-1} \left(1 + \left(\frac{D_h}{L_e}\right)^{\frac{2}{3}}\right)$	[71],[72]
Plain Triangular Fin	$Re_{D_h} > 2300$ $0.5 < Pr_{D_h} < 2000$	$Nu_{D_h} = \frac{f_D}{2}\left(Re_{D_h} - 1000\right) Pr_{D_h} \left(1 + 12.7\left(\frac{f_D}{2}\right)^{0.5}\left(Pr_{D_h}^{\frac{2}{3}} - 1\right)\right)^{-1} \left(1 + \left(\frac{D_h}{L_e}\right)^{\frac{2}{3}}\right)$	[71],[72]
Wavy Fin	$Re_{D_h} < 1900$	$j = 0.2951\, Re_{D_h}^{-0.1908} \left(\frac{p}{D_h}\right)^{0.7356} \left(\frac{H_c}{D_h}\right)^{0.1378} \left(\frac{t}{D_h}\right)^{0.0485} \left(\frac{2A}{D_h}\right)^{0.2467} \left(\frac{L}{D_h}\right)^{-0.4976}$	[73]
	$Re_{D_h} > 1900$	$j = 0.7293\, Re_{D_h}^{-0.3637} \left(\frac{p}{D_h}\right)^{0.7966} \left(\frac{H_c}{D_h}\right)^{0.2398} \left(\frac{L}{D_h}\right)^{-0.4979} \left(\frac{t}{D_h}\right)^{0.0402} \left(\frac{2A}{D_h}\right)^{0.2012} \left(\frac{L_e}{D_h}\right)^{-0.3026}$	
Offset strip Fin	$Re_{D_h} < 2000$	$j = 1.37\, Re_{D_h}^{-0.67} \left(\frac{L_s}{D_h}\right)^{-0.25} \left(\frac{B_c}{H_c}\right)^{-0.184}$	[74]
	$Re_{D_h} \geq 2000$	$j = 1.17\, Re_{D_h}^{-0.36} \left(\frac{L_s}{D_h} + 3.75\right)^{-1} \left(\frac{t}{D_h}\right)^{0.089}$	
Louvred (Triangular) Fin		$j = 0.65842 \left(\frac{L_e}{L_l\, Re_L\, Pr_{D_h}}\right)^{0.6317} \left(\frac{L_l}{H_c}\right)^{-0.4825} \left(\frac{L_e}{H_c}\, tan(L_a)\right)^{-0.433} \left(\frac{L_s}{t}\right)^{-1.1902}$	[75]
Perforated (Rectangular) Fin	Nu_{SF} (solid fin) is calculated as is done with Plain Rectangular Fin		[76],[77]
	$P_d > 0.04$	$Nu_{PF} = Nu_{SF}\, 1.296\; Re_{D_{SF}}^{-0.0357} (1 - P)^{0.269}$	
	$P_d < 0.04$	$Nu_{PF} = Nu_{SF}\left(0.0307\; Re_{D_{SF}}^{0.226} + 0.583(1 - P)^{0.704}\right)$	

A. 3. Pressure drop correlations (channel flow)

Pressure drop correlations (in terms of f_D or f_F) are available for the different geometries at different operating conditions. The most relevant ones for this study are presented in Table A.3:

Table A.3. Pressure drop correlations in terms of Darcy friction factor (f_D) or Fanning friction factor (f_F) for the different compact geometries analysed.

Receiver	Validity	Correlation	Reference
Plain Rectangular Fin	$2700 < Re_{D_h} < 10100$	$f_F = 0.059\ Re_{D_h}^{-0.117} \left(\frac{t}{H_c}\right)^{0.118} \left(\frac{p}{H_c}\right)^{-0.253} \left(\frac{L_e}{D_h}\right)^{-0.147}$	[69],[78]
	$Re_{D_h} > 10100$ $0.5 < Pr_{D_h} < 2000$	$f_D = (1.82\ log10(Re_{D_h}) - 1.64)^{-2}$	[71],[72]
Plain Triangular Fin	$Re_{D_h} > 2300$ $0.5 < Pr_{D_h} < 2000$	$f_D = (1.82\ log10(Re_{D_h}) - 1.64)^{-2}$	[71],[72]
Wavy Fin	$Re_{D_h} < 1900$	$f_F = 38.7488\ Re_{D_h}^{-0.3840} \left(\frac{p}{D_h}\right)^{-1.479} \left(\frac{H_c}{D_h}\right)^{-0.3696} \left(\frac{L}{D_h}\right)^{-1.4542} \left(\frac{t}{D_h}\right)^{0.1016} \left(\frac{2A}{D_h}\right)^{1.0903} \left(\frac{L_e}{D_h}\right)^{-0.1549}$	[73]
	$Re_{D_h} > 1900$	$f_F = 52.2375\ Re_{D_h}^{-0.3524} \left(\frac{p}{D_h}\right)^{-1.6277} \left(\frac{H_c}{D_h}\right)^{-0.3529} \left(\frac{L}{D_h}\right)^{-1.7484} \left(\frac{t}{D_h}\right)^{0.1034} \left(\frac{2A}{D_h}\right)^{1.2294} \left(\frac{L_e}{D_h}\right)^{-0.2371}$	
Offset strip Fin	$Re_{D_h} < 2000$	$f_F = 5.55\ Re_{D_h}^{-0.67} \left(\frac{L_s}{D_h}\right)^{-0.32} \left(\frac{B_c}{H_c}\right)^{-0.092}$	[74]
	$Re_{D_h} \geq 2000$	$f_F = 0.83\ Re_{D_h}^{-0.20} \left(\frac{L_s}{D_h} + 0.33\right)^{-0.5} \left(\frac{t}{D_h}\right)^{0.534}$	
Louvred (Triangular) Fin		$f_F = 0.07667 \left(\frac{L_e}{L_l\ Re_L\ Pr_D}\right)^{0.3211} \left(\frac{L_l}{H_c}\right)^{-2.0217} \left(tan(L_a)\right)^{-2.3501} \left(\frac{L_s}{t}\right)^{-2.5343}$	[75]
Perforated (Rectangular) Fin	The solid fin pressure drop is calculated as was the Plain Rectangular Fin's and its ratio with perforated fins is taken as: $\Delta p_{PF} = \Delta p_{SF}\ \ (0.97 - Re_{D_{SF}}\ 10^{-5})$		[76],[77]